First Results from the *Herschel* and ALMA Spectroscopic Surveys of the SMC: The Relationship between [C II]-bright Gas and CO-bright Gas at Low Metallicity[*]

Katherine E. Jameson[1,2] , Alberto D. Bolatto[1] , Mark Wolfire[1], Steven R. Warren[3], Rodrigo Herrera-Camus[4] ,
Kevin Croxall[5,6] , Eric Pellegrini[7], John-David Smith[8] , Monica Rubio[9], Remy Indebetouw[10,11] , Frank P. Israel[12] ,
Margaret Meixner[13], Julia Roman-Duval[13] , Jacco Th. van Loon[14] , Erik Muller[15], Celia Verdugo[16], Hans Zinnecker[17,18], and
Yoko Okada[19]

[1] Astronomy Department and Laboratory for Millimeter-wave Astronomy, University of Maryland, College Park, MD 20742, USA; katie.jameson@anu.edu.au
[2] Research School of Astronomy and Astrophysics, Australian National University, Canberra ACT 2611, Australia
[3] Cray, Inc., 380 Jackson Street, Suite 210, St. Paul, MN 55101, USA
[4] Max-Planck-Institut für extraterrestrische Physik, Giessenbachstr., D-85748 Garching, Germany
[5] Department of Astronomy, The Ohio State University, 4051 McPherson Laboratory, 140 West 18th Avenue, Columbus, OH 43210, USA
[6] Illumination Works LLC, 5650 Blazer Parkway, Suite 152, Dublin OH 43017, USA
[7] Zentrum für Astronomie, Institut für Theoretische Astrophysik, Universität Heidelberg, D-69120 Heidelberg, Germany
[8] Department of Physics & Astronomy, University of Toledo, 2801 W. Bancroft Street, Toledo, OH 43606, USA
[9] Departamento de Astronomía, Universidad de Chile, Casilla 36-D, Chile
[10] Department of Astronomy, University of Virginia, P.O. Box 400325, Charlottesville, VA 22904, USA
[11] National Radio Astronomy Observatory, 520 Edgemont Road, Charlottesville, VA 22903, USA
[12] Sterrewacht Leiden, Leiden University, P.O. Box 9513, 2300 RA Leiden, The Netherlands
[13] Space Telescope Science Institute, 3700 San Martin Drive, Baltimore, MD 21218, USA
[14] Lennard-Jones Laboratories, Keele University, Staffordshire ST5 5BG, UK
[15] National Astronomical Observatory of Japan, Chile Observatory, 2-21-1 Osawa, Mitaka, Tokyo 181-8588, Japan
[16] The Joint ALMA Observatory, Alonso de Crdova 3107, Vitacura, Santiago, Chile
[17] Deutsches SOFIA Institut, Univ. of Stuttgart, Pfaffenwaldring 29, 70569 Stuttgart, Germany
[18] Universidad Autónoma de Chile, Pedro de Valdivia 425, Providencia, Chile
[19] I. Physikalisches Institut der Universität zu Köln, Zülpicher Straße 77, D-50937, Köln, Germany

Abstract

The Small Magellanic Cloud (SMC) provides the only laboratory to study the structure of molecular gas at high resolution and low metallicity. We present results from the *Herschel* Spectroscopic Survey of the SMC (HS^3), which mapped the key far-IR cooling lines [C II], [O I], [N II], and [O III] in five star-forming regions, and new ALMA 7 m array maps of ^{12}CO and ^{13}CO $(2 - 1)$ with coverage overlapping four of the five HS^3 regions. We detect [C II] and [O I] throughout all of the regions mapped. The data allow us to compare the structure of the molecular clouds and surrounding photodissociation regions using ^{13}CO, ^{12}CO, [C II], and [O I] emission at $\lesssim 10''$ (<3 pc) scales. We estimate A_V using far-IR thermal continuum emission from dust and find that the CO/[C II] ratios reach the Milky Way value at high A_V in the centers of the clouds and fall to $\sim 1/5$–$1/10\times$ the Milky Way value in the outskirts, indicating the presence of translucent molecular gas not traced by bright ^{12}CO emission. We estimate the amount of molecular gas traced by bright [C II] emission at low A_V and bright ^{12}CO emission at high A_V. We find that most of the molecular gas is at low A_V and traced by bright [C II] emission, but that faint ^{12}CO emission appears to extend to where we estimate that the H$_2$-to-H I transition occurs. By converting our H$_2$ gas estimates to a CO-to-H$_2$ conversion factor (X_{CO}), we show that X_{CO} is primarily a function of A_V, consistent with simulations and models of low-metallicity molecular clouds.

Key words: galaxies: dwarf – galaxies: evolution – ISM: clouds – Magellanic Clouds

Supporting material: data behind figures

1. Introduction

Molecular clouds are the sites of the first stages of star formation. The structure of molecular clouds and the transition from atomic to molecular gas can affect what fraction of the gas participates in star formation. The effects of metallicity on the structure and properties of molecular clouds (Rubio et al. 1993b; Bolatto et al. 2008; Heyer et al. 2009; Hughes et al. 2010; Schruba et al. 2012), and the resulting effects on star formation, are not well understood owing to the difficulty in observing H$_2$ and the molecular-to-atomic transition at low metallicity. Without knowledge of these effects, simulations of

molecular clouds and star formation at low metallicity are largely unconstrained. Galaxy evolution simulations, particularly at the very early times when metallicities are low, rely on an accurate understanding of the fraction of gas available for star formation. At a metallicity of $Z \sim 1/5\,Z_\odot$ (Dufour 1984; Kurt et al. 1999; Pagel 2003) and a distance of $D \approx 63$ kpc, the Small Magellanic Cloud (SMC) provides an ideal laboratory to study the effects of low metallicity on the molecular gas and the molecular-to-atomic transition.

The transition from atomic to molecular gas occurs at the outer edges of the molecular cloud, where the shielding is lower and molecules are more easily dissociated. These edges are referred to as photodissociation regions (PDRs). Studying the molecular gas structure requires understanding the distribution of H$_2$ from the dense cloud cores to the diffuse

outer layers of the clouds. The most common tracer of molecular gas is ^{12}CO. At low metallicity, the dissociating far-UV (FUV) radiation field strengths are higher because there is less dust to shield the molecular gas. The H_2 gas, however, is expected to be more prevalent than CO owing to the ability of H_2 to more effectively self-shield against dissociating FUV photons. While more prevalent, the lowest-energy line transition arising directly from H_2 has a temperature-equivalent energy of $E_u/k = 510$ K and critical density of $n_{crit,H} \sim 1000$ cm^{-2}, which will trace only warm ($T \gtrsim 100$ K) molecular gas. Both observations and modeling suggest that $\sim 30\%$–50% of the H_2 in the solar neighborhood resides in a "CO-faint" phase (e.g., Grenier et al. 2005; Wolfire et al. 2010; Planck Collaboration et al. 2011). Studies of the SMC suggest this phase to encompass 80%–90% of all the H_2 (Israel 1997; Pak et al. 1998; Leroy et al. 2007, 2011; Bolatto et al. 2011), likely dominating the molecular reservoir available to star formation.

In regions where CO is photodissociated, the carbon is present as neutral carbon, C^0, and singly ionized carbon, C^+. Given the CO dissociation energy of 10.6 eV and the C ionization potential of 11.3 eV, a large fraction of the carbon will be ionized throughout the interstellar medium (ISM). The [C II] 158 μm line (arising from the $^2P^0_{3/2} \rightarrow ^2P^0_{1/2}$ fine-structure transition), with an energy above ground of $\Delta E/k = 91$ K, originates from the "CO-faint" H_2 gas, as well as the neutral atomic and ionized gas. The [C II] line thus offers the potential to estimate the amount of molecular gas not traced by bright CO emission, particularly in low-metallicity environments, where a significant fraction of the H_2 may not be traced by bright CO emission: after removing the contributions to [C II] from atomic and ionized gas, the remaining emission can be attributed to molecular gas. To then convert the [C II] emission to a molecular gas column density requires some knowledge of the conditions of the gas (namely, volume density and temperature, which determine the [C II] excitation). Early [C II] observations of low-metallicity environments from the Kuiper Airborne Observatory have shown bright emission and high [C II]/CO ratios that are best explained by a significant amount of H_2 not traced by CO emission in star-forming regions of the Magellanic Clouds (Poglitsch et al. 1995; Israel et al. 1996; Israel & Maloney 2011) and IC 10 (Madden et al. 1997). Even at higher metallicity in the Milky Way, spectral decomposition of the [C II] line using the GOT C + survey shows that molecular gas not associated with bright CO emission (called "CO-dark" or "CO-faint" molecular gas) accounts for $\sim 30\%$ of the total molecular mass (Pineda et al. 2013; Langer et al. 2014).

To estimate the total amount of molecular gas, we need both [C II] and CO observations: the [C II] emission traces the molecular gas in the outer parts of the cloud within the PDR, while the CO emission traces the remaining molecular gas in the denser, inner regions of the cloud. One way to trace the depth probed along the line of sight is to use the visual extinction due to dust, A_V. Low A_V indicates a lower column of dust and gas associated with diffuse gas and the PDR region in the outskirts of molecular clouds. Higher A_V indicates a higher column of dust and gas and the transition into the denser regions of molecular clouds. In terms of A_V, [C II] will trace the molecular gas at low A_V and CO will trace the molecular gas at high A_V. The existing CO data have only traced the high A_V molecular gas. The Magellanic Clouds have been studied extensively in CO with earliest surveys completed using the

Columbia 1.2 m (Cohen et al. 1988; Rubio et al. 1991). Since then, many higher-resolution surveys of the SMC have taken place using Nanten (Mizuno et al. 2001), the Swedish ESO Submillimetre Telescope (SEST; Israel et al. 1993; Rubio et al. 1993b), and Mopra (Muller et al. 2010). Their typical angular resolution of $\sim 30''$ (~ 10 pc), however, makes it difficult to use them to study individual star-forming regions.

In this study, we present new *Herschel* far-IR (FIR) line observations, including Photoconductor Array Camera and Spectrometer (PACS) [C II] and [O I] observations, from the *Herschel* Spectroscopic Survey of the SMC (HS^3), together with new ALMA *Morita-san* Compact Array (ACA) ^{12}CO, ^{13}CO, and $C^{18}O$ observations of the Southwest Bar of the SMC, all at a resolution of $\sim 5''$–$10''$ (~ 1.5–3 pc). The ACA resolution is similar to that of the PACS spectroscopy, which allows us to produce estimates of molecular gas from [C II] and CO at comparable resolutions and investigate how the "[C II]-bright" molecular gas relates to the "CO-bright" molecular gas at low metallicity.

In Section 2 we describe the details of the HS^3 and ALMA SMC observations and data reduction, as well as ancillary data used for this study. We present the main results of the two surveys in Section 3. Our methodology to estimate molecular gas using [C II] and ^{12}CO emission is described in Section 4. We discuss the results of our new molecular gas estimates in Section 5, including a comparison to previous dust-based estimates and converting our estimates to CO-to-H_2 conversion factor values to compare to models and simulations of molecular clouds at low metallicity. Finally, Section 6 summarizes our work and outlines the main conclusions of this study.

2. Observations

2.1. The Herschel Spectroscopic Survey of the SMC

The HS^3 (Pilbratt et al. 2010) maps the key FIR lines of [C II] 158 μm, [O I] 63 μm, [O III] 88 μm, and [N II] 122 μm with the PACS spectrometer (Poglitsch et al. 2010) and obtain Spectral and Photometric Imaging Receiver (SPIRE; Griffin et al. 2010) Fourier Transform Spectrometer (FTS) observations (which include [N II] 205 μm) in five regions across the SMC with varying star formation activity and ISM conditions. These targets were covered using strips oriented to span the range from the predominantly molecular to the presumably atomic regime. The strips are fully sampled in [C II] and [O I], while only a few pointings were observed for [N II] and [O III].

The HS^3 targeted regions span a range of star formation activity, overlapping with the *Spitzer* Spectroscopic Survey of the SMC (S^{4}MC; Sandstrom et al. 2012) whenever possible, and cover a range of "CO-faint" molecular gas fraction using dust-based molecular gas estimates (Bolatto et al. 2011) going from the peaks out to the more diffuse gas. The main survey covers five star-forming areas, which we refer to as "N83" (also includes N84), "SWBarN" (covers N27), "SWBarS" (covers N13), "N22" (also includes N25, N26, H36, and H35), and a smaller square region called "SWDarkPK" that covers a region with a dust-based peak in the molecular gas without any associated CO emission as seen in the NANTEN ^{12}CO map (Mizuno et al. 2001). The "N" numbered regions refer to H II regions from the catalog by Henize (1956), and the "H" numbered regions are from the catalog of Hα structures by Davies et al. (1976).

Table 1
HS³ [C II] and [O I] Map Properties

| Region | Center Position | | Size | P.A. | 1σ Uncertainty $(10^{-9}\ \mathrm{W\ m^{-2}\ sr^{-1}})$ | |
	R.A. (J2000)	Decl. (J2000)			[C II]	[O I]
SWBarS	$00^\mathrm{h}45^\mathrm{m}27\overset{s}{.}10$	$-73^\mathrm{d}21^\mathrm{m}00\overset{s}{.}00$	$1\overset{'}{.}7 \times 6\overset{'}{.}1$	$10°$	1.2	4.1
N22	$00^\mathrm{h}47^\mathrm{m}58\overset{s}{.}10$	$-73^\mathrm{d}16^\mathrm{m}52\overset{s}{.}13$	$1\overset{'}{.}7 \times 6\overset{'}{.}1$	$20°$	1.4	3.5
SWBarN	$00^\mathrm{h}48^\mathrm{m}26\overset{s}{.}88$	$-73^\mathrm{d}06^\mathrm{m}04\overset{s}{.}36$	$1\overset{'}{.}7 \times 6\overset{'}{.}1$	$145°$	1.5	3.9
SWDarkPK	$00^\mathrm{h}52^\mathrm{m}23\overset{s}{.}70$	$-73^\mathrm{d}14^\mathrm{m}49\overset{s}{.}00$	$1\overset{'}{.}2 \times 1\overset{'}{.}2$	$48°$	1.3	3.4
N83	$01^\mathrm{h}14^\mathrm{m}19\overset{s}{.}28$	$-73^\mathrm{d}15^\mathrm{m}09\overset{s}{.}04$	$1\overset{'}{.}7 \times 8\overset{'}{.}0$	$30°$	1.4	3.5

Table 2
HS³ [N II] and [O III] Map Properties

| Region | Center Position | | Size | P.A. | | 1σ Uncertainty $(10^{-9}\ \mathrm{W\ m^{-2}\ sr^{-1}})$ | |
	R.A. (J2000)	Decl. (J2000)		[N II]	[O III]	[N II]	[O III]
SWBarS	$00^\mathrm{h}45^\mathrm{m}21\overset{s}{.}85$	$-73^\mathrm{d}22^\mathrm{m}49\overset{s}{.}36$	$1\overset{'}{.}5 \times 1\overset{'}{.}5$	$75°$	$10°$	0.34	2.8
N22	$00^\mathrm{h}47^\mathrm{m}54\overset{s}{.}35$	$-73^\mathrm{d}17^\mathrm{m}27\overset{s}{.}69$	$1\overset{'}{.}5 \times 1\overset{'}{.}5$	$65°$	$40°$	0.36	2.8
SWBarN	$00^\mathrm{h}48^\mathrm{m}26\overset{s}{.}30$	$-73^\mathrm{d}06^\mathrm{m}04\overset{s}{.}28$	$1\overset{'}{.}5 \times 1\overset{'}{.}5$	$75°$	$55°$	0.27	2.4
SWDarkPK	$00^\mathrm{h}52^\mathrm{m}56\overset{s}{.}11$	$-73^\mathrm{d}12^\mathrm{m}17\overset{s}{.}25$	$1' \times 1'$	$55°$	$40°$	0.33	2.8
N83	$01^\mathrm{h}14^\mathrm{m}03\overset{s}{.}28$	$-73^\mathrm{d}17^\mathrm{m}06\overset{s}{.}81$	$1\overset{'}{.}5 \times 1\overset{'}{.}5$	$50°$	$65°$	0.29	3.0

The [C II] and [O I] maps are strips that encompass the peaks in CO, star formation, and "CO-faint" H₂ as traced by dust. Using the PACS spectrometer $47'' \times 47''$ field of view, the strips were sampled using rasters with sizes $33'' \times 11$ ([C II]) and $24'' \times 15$ ([O I]) by $23\overset{''}{.}5 \times 3$. Both [O III] and [N II] observations were targeted at the location of the main ionizing source in each region and sampled with $23\overset{''}{.}5 \times 2$ by $23\overset{''}{.}5 \times 2$ raster. The PACS maps used the unchopped scan mode with a common absolute reference position placed south of the SMC "Wing" and observed at least once every 2 hr. The PACS spectrometer has a beam FWHM of $\theta \sim 9\overset{''}{.}5$ at the wavelength for [O I] (63 μm) and [O III] (88 μm), $\theta \sim 10''$ at [N II] (122 μm), and $\theta \sim 12''$ at [C II] (158 μm), which have corresponding spectral resolutions of ~100, 120, 320, and 230 km s⁻¹ (Poglitsch et al. 2010). Tables 1 and 2 list the positions and uncertainties for all the PACS spectroscopy line images. The SPIRE FTS observations were "intermediate sampling" single pointing (with a $2'$ circular field of view) at high resolution at the star-forming peak, which is typically close to the peak in ¹²CO, for the N83, SWBarN, SWBarS, and N22 regions. In addition to the main survey region FTS observations, one single pointing covered the brightest H II region N66, which has PACS [C II] and [O I] observations as part of Guaranteed Time Key Project SHINING and is included in the *Herschel* Dwarf Galaxy Survey (DGS; Madden et al. 2013).

2.1.1. Data Reduction

PACS spectral observations were obtained in the unchopped mapping mode and reduced using the Herschel Interactive Processing Environment (HIPE) version 12.0.2765 (Ott 2010). Reductions applied the standard spectral response functions and flat-field corrections and flagged instrument artifacts and bad pixels (see Poglitsch et al. 2010; Croxall et al. 2012). The dark current, determined from each individual observation, was subtracted during processing, as it was not removed via chopping. *Herschel*'s baseline exhibits significant baseline drifts, and distinctive instrumental transients are common occurrences. These instabilities result in a variable nonastrophysical continuum, which is dominated by emission from *Herschel* itself.

Transient signals are strongly correlated with motions of the PACS grating and of *Herschel*. Using fits of the Draine & Li (2007) dust model to spectral energy distributions (SEDs) of galaxies in the KINGFISH sample, we estimate that the expected astrophysical continuum is less than 2% of the spectral continuum detected at [C II] 158 μm. Given that the other spectral lines were located farther from the peak of the dust continuum than the [C II] line, we assume that thermal dust emission is undetected in the PACS spectra. Thus, the continuum adjacent to the expected locations of the observed fine-structure lines should be constant and is used to correct for transients. This has significantly improved our ability to detect line emission.

The averages of the clean off-observations obtained were subtracted from observations to correct for the thermal background contributed by *Herschel*. Subsequently, all spectra within a given spatial element were combined. Final spectral cubes with $2\overset{''}{.}06$ spatial pixels were created by combining individual pointings using the Drizzle algorithm implemented in HIPE. In-flight flux calibrations[20] were applied to the data. These calibrations resulted in absolute flux uncertainties on the order of 15% with relative flux uncertainties between each *Herschel* pointing on the order of ~10%.

The long- and short-wavelength SPIRE FTS arrays (FWHMs of $34''$ and $19''$, respectively) are arranged in concentric circles and are dithered 4 times to provide complete coverage of the mapped region. The FTS data reduction started with level 0.5 data, which was temperature drift corrected, detector clipped, and time shift corrected using HIPE (version 11). A semi-extended-source correction (Wu et al. 2013) was applied to the individual bolometer (level 1) data before mapping. Spectral cubes were produced using the corrected bolometer fluxes.

---

[20] Calibration Version 65.

2.2. ALMA Survey of the Southwest Bar

We mapped four regions in the Southwest Bar of the SMC in ^{12}CO, ^{13}CO, and $C^{18}O$ $(2-1)$ using Band 6 of the ALMA Atacama Compact Array (ACA; 7 m array consisting of 11 antennas) and Total Power array (TP; 12 m single-dish) during Cycle 2. Three of these regions were previously mapped in ^{12}CO and ^{13}CO $(2-1)$ using SEST (Rubio et al. 1993a, 1993b, 1996), but at a resolution of $22''$. The ACA maps were observed using a mosaic with $22''1$ spacing of 47 pointings for the N22, SWBarS, and SWBarN regions and 52 pointings for the SWDarkPK with 25.5 s integration time per pointing. Both ^{12}CO and ^{13}CO were observed with 117.2 MHz (152 km s^{-1}) bandwidth and 121.15 kHz (0.2 km s^{-1}) spectral resolution. We chose a somewhat broader bandwidth for $C^{18}O$ of 468.8 MHz (642 km s^{-1}) and corresponding 0.24 MHz (0.12 km s^{-1}) spectral resolution, and we used the fourth spectral window for continuum (1875.0 MHz bandwidth, 7.81 MHz resolution). During the early ALMA cycles, the fast-mapping capabilities of the array were fairly limited, and so we decided to cover only half of the strips mapped by HS^3. The coverage of the maps overlaps approximately with the main CO emission known to be present in the strips, except for SWDarkPK, where the PACS map is small and we covered its entire area.

We used the Common Astronomy Software Applications (CASA; McMullin et al. 2007) package to reduce, combine, and image the data. The ACA data were calibrated with the pipeline using CASA version 4.2.2, and no modifications were made to the calibration script. We used the calibrated delivered TP data, which were manually calibrated using CASA version 4.5.0 (described in the official CASA guide), with the exception of the SWBarN ^{12}CO spectral window (SPW 17). For the SWBarN SPW 17 we modified the baseline subtraction in the calibration script to avoid channels with line emission (the delivered calibration script included all channels when fitting the baseline). We created the reduced measurement set using the script provided with the delivered ACA data and use the imaged TP SPWs as part of the delivered data.

We cleaned each spectral window of the ACA data and imaged it using CLEAN, and then we used FEATHER to combine the ACA images with the corresponding TP image regridded to match the ACA data (using CASA version 4.7.0). We used Briggs weighting with a robust parameter of 0.5 and cleaned to $\sim 2.5 \times$ rms found away from strong emission in the dirty data cube. As there was no noticeable continuum emission, the effect of continuum subtraction was negligible, and we did not include any continuum subtraction for the final imaged cubes. Due to the short integration times and the arrangement of the 7 m array, we used conservative masks for cleaning to reduce the effects of the poor $u-v$ coverage of the ACA-only data. The data were imaged at 0.3 km s^{-1} spectral resolution with synthesized beam sizes of $\sim 7'' \times 5''5$ (2.1 pc $\times$ 1.7 pc) for ^{12}CO $(2-1)$. The combination of the ACA and TP data make the observations sensitive to all spatial scales. The previously published single-dish SEST ^{12}CO $(2-1)$ data from Rubio et al. (1993a) overlap with the SWBarN region, which they refer to as LIRS49. They found a peak temperature of 2.56 K in a $43''$ beam at $\alpha(B1950) = 00^h46^m33^s$, $\delta(B1950) = -73^d22^m00^s$, and we find a peak temperature of 2.55 K in the same aperture in the SWBarN ACA+TP data when convolved to $43''$ resolution. The positions, beam sizes, and sensitivities of the observations are listed in Tables 3 and 4.

Table 3
ALMA ACA+TP Map Properties

Region	Map Center R.A. (J2000)	Decl. (J2000)	Map Size	P. A.
SWBarS	$00^h45^m24^s54$	$-73^d21^m42^s63$	$2'3 \times 3'5$	$10°$
N22	$00^h47^m54^s28$	$-73^d17^m46^s76$	$2'3 \times 3'5$	$20°$
SWBarN	$00^h48^m15^s53$	$-73^d04^m56^s41$	$2'3 \times 3'5$	$145°$
SWDarkPK	$00^h52^m56^s07$	$-73^d12^m17^s08$	$3' \times 3'$	$48°$

2.3. H I Data

The neutral atomic gas data come from 21 cm line observations of H I. We use the H I map from Stanimirović et al. (1999) that combined Australian Telescope Compact Array (ATCA) and Parkes 64 m radio telescope data. The interferometric ATCA data set the map resolution at $1'6$ ($r \sim 30$ pc in the SMC), but the data are sensitive to all size scales owing to the combination of interferometric and single-dish data. The observed brightness temperature of the 21 cm line emission is converted to H I column density (N_{HI}) assuming optically thin emission. The observed brightness temperature of the 21 cm line emission is converted to H I column density (N_{HI}) using

$$N_{HI} = 1.823 \times 10^{18} \frac{cm^{-2}}{K\ km\ s^{-1}} \int T_B(v)\, dv.$$

The SMC map has an rms column density of 5.0×10^{19} cm^{-2}. While most of the H I emission is likely optical thin, some fraction will be optically thick, and the optically thin assumption will cause us to underestimate N_{HI}. Stanimirović et al. (1999) produced a statistical correction to account for optically thick H I line emission in the SMC; however, the correction is based only on 13 H I absorption measurements, with only two in the Southwest Bar. We choose not to apply the correction since it has little effect on our H$_2$ estimate from [C II] (see Section 4.2).

2.4. Additional Data

We use mid-infrared *Spitzer* IRAC and MIPS data from the SMC-SAGE (Gordon et al. 2011) and S^{3}MC (Bolatto et al. 2007) surveys and spectroscopic IRS data, particularly H$_2$ rotational lines, from the S^{4}MC (Sandstrom et al. 2012) survey. The maps of the H$_2$ rotational line images were produced by fitting and removing the baseline near the line and then calculating the total line intensity. We also use a velocity-resolved [C II] spectrum from the GREAT heterodyne instrument (Heyminck et al. 2012) on board the Stratospheric Observatory for Infrared Astronomy (SOFIA; Temi et al. 2014) from the SMC survey presented in R. Herrera-Camus et al. (2017, in preparation).

Since the ALMA Survey focuses on the Southwest Bar of the SMC, there is no comparable map of CO from ALMA for N83. However, there are new APEX[21] maps of ^{12}CO $(2-1)$ that overlap the N83 HS^3 region (PI: Rubio). We use the APEX data for the N83 region to be able to make similar comparisons

---

[21] This publication is based on data acquired with the Atacama Pathfinder Experiment (APEX). APEX is a collaboration between the Max-Planck-Institut fur Radioastronomie, the European Southern Observatory, and the Onsala Space Observatory.

Table 4
ALMA ACA+TP Map Properties (continued)

Region	$\theta_{\mathrm{maj}}('') \times \theta_{\mathrm{min}}('')$			rms (K)		
	^{12}CO	^{13}CO	C^{18}O	^{12}CO	^{13}CO	C^{18}O
SWBarS	6.60×6.06	6.92×6.05	6.76×6.18	0.17	0.16	0.10
N22	6.39×5.56	6.59×5.83	7.01×6.41	0.24	0.22	0.13
SWBarN	7.08×5.74	7.25×5.33	7.40×5.66	0.12	0.16	0.08
SWDarkPK	6.95×5.55	8.39×5.63	7.42×5.72	0.18	0.16	0.10

to the HS3^3 data, but note that the lower resolution ($\sim 25''$) limits the analysis. To do this, we take the additional step of convolving and re-gridding the *Herschel* spectroscopic maps ([O I], [C II]) to match that of the APEX ^{12}CO $(2 - 1)$ map.

2.5. Total-infrared

We determine the total-infrared (TIR) intensity (from 3 to 1100 μm) using the *Spitzer* 24 and 70 μm (no *Herschel* 70 μm map exists) from SMC-SAGE (Gordon et al. 2011) combined with *Herschel* 100, 160, and 250 μm images from HERITAGE (Meixner et al. 2013). All of the images are convolved to the lowest resolution of the *Spitzer* 70 μm image ($\sim 18''$) using the convolution kernels from Aniano et al. (2011). The TIR intensity is calculated following the prescription by Galametz et al. (2013):

$$S_{\mathrm{TIR}} = \sum c_i S_i, \qquad (1)$$

all in units of W kpc^{-2}, where the coefficients (c_i) are 2.013, 0.508, 0.393, 0.599, and 0.680 for 24, 70, 100, 160, and 250 μm, respectively.

2.6. Estimating A_V

We investigate the structure of the PDR and molecular cloud by using the visual extinction (A_V) as an indicator of the total column through the cloud and to gauge the depth within the cloud associated with the observations. To match the high resolution of the [C II], [O I], and ALMA CO data, we use the optical depth at 160 μm (τ_{160}) and the HERITAGE 160 μm map of the SMC (Meixner et al. 2013) as the basis for producing a map of A_V. Lee et al. (2015) fit a modified blackbody with $\beta = 1.5$ to the SMC HERITAGE 100, 160, 250, and 350 μm data for the SMC. We re-sample their map of fitted dust temperatures at the lower resolution of the 350 μm *Herschel* map ($\sim 30''$) to the higher-resolution 160 μm map ($\sim 12''$) in order to estimate τ_{160} at a resolution comparable to the [C II] and ALMA CO maps. We convert from τ_{160} to A_V using $A_V \sim 2200\tau_{160}$ from Lee et al. (2015), which is based on measurements in the Milky Way and provides similar A_V values to those found using UV/optical and NIR color excess methods (see Figure 1 in Lee et al. 2015). We stress that these values of A_V are estimates that include uncertainties associated with the assumptions made in the dust modeling (e.g., the assumption of a single dust temperature) and the conversion from τ_{160} to A_V. While the extinction at ~ 11 eV (ionization potential of carbon) would be a more relevant quantity to our study of [C II] and CO emission, the conversion from τ_{160} to A_{11eV} is highly uncertain.

3. Results

We present the high-resolution imaging ($\sim 10''$ ~ 3 pc) of a suite of FIR cooling lines from HS^3 and CO from the ALMA

ACA in the SMC. [C II] and [O I] lines were detected in all of the regions targeted, and [C II] is detected throughout all of the regions. The ALMA ACA+TP data show clear detections of ^{12}CO and ^{13}CO $(2 - 1)$ emission in all of the regions, but C^{18}O is not detected. In this section we discuss the comparison of the [O I], [C II], and ^{12}CO emission.

3.1. [C II] and [O I]

The [C II] 158 μm line dominates the cooling of the warm ($T \sim 100$ K) neutral gas because of the high carbon abundance, its lower ionization potential of 11.26 eV, and an energy equivalent temperature of 92 K. Ionized carbon, C$^+$, exists throughout most phases of the ISM except in the dense molecular gas, where most of the carbon is locked in CO. The [O I] 63 μm line also contributes to the gas cooling, but with an energy equivalent temperature of 228 K and a high critical density ($\sim 10^5$ cm^{-3}); this line dominates over the [C II] emission only in the densest gas. Indeed, the bright "blue" knots of [O I] emission in Figure 1 are coincident with bright knots of Hα emission (in black contours) associated with very recent massive star formation in dense and presumably warm structures bathed by intense radiation. Oxygen can remain neutral in regions with ionized hydrogen and Hα emission owing to its slightly higher ionization potential of 13.62 eV. In warm PDRs subjected to radiation fields larger than 10^3 Habings and due to the difference in critical densities, the [O I]-to-[C II] ratio is a good indicator of density, but in colder gas and particularly below $n \lesssim 10^4$ cm^{-3} it is mostly sensitive to temperature and the incident radiation field (e.g., Kaufman et al. 1999).

Figure 1 shows the [O I] and [C II] integrated intensity images in combination with the 160 μm PACS image showing dust continuum emission. The differences in the local star formation, shown by Hα in black contours, produce different structures and varying intensities of [C II], [O I], and dust emission. In many faint [C II] regions in the diffuse gas the [O I] line is detected (see inset spectra in Figure 1). In principle, it is possible for [O I] 63 μm to be a very important coolant for the warm neutral medium (WNM) of the ISM (Wolfire et al. 1995, 2003). Despite the high critical density of this transition, the high temperature of the WNM excites [O I], making it an efficient coolant even in $n \sim 1$ cm^{-3} gas.

3.1.1. [O I] Self-absorption

A challenge with interpreting velocity-unresolved observations of [O I] 63 μm, such as ours ($\Delta v \sim 100$ km s^{-1}), is the potential effect of self-absorption or absorption from cold gas along the line of sight, a phenomenon originally identified through anomalous [O I] 145 μm/63 μm integrated line ratios. Indeed, some Milky Way massive star-forming regions show significant self-absorption and absorption by foreground cold
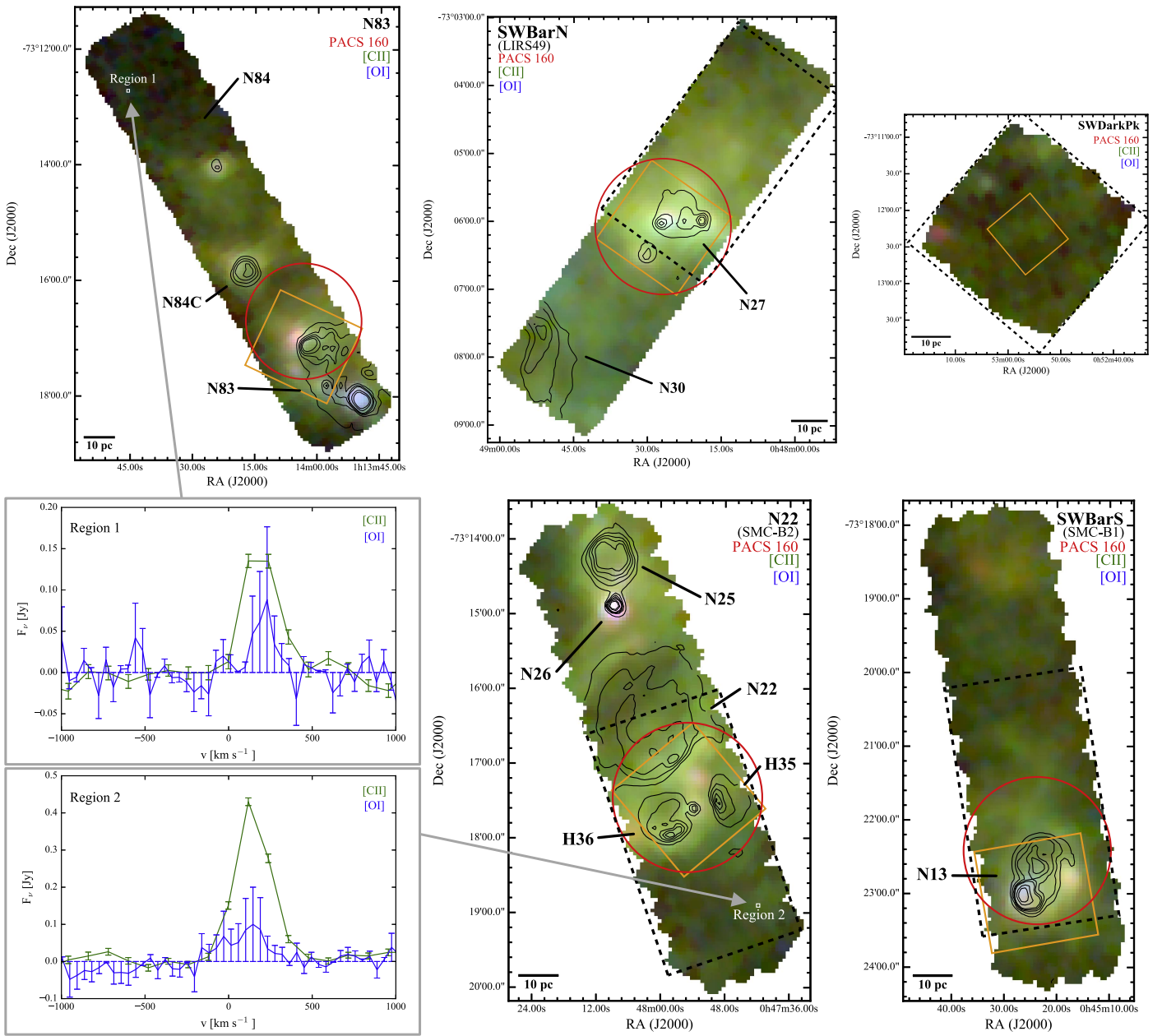
Figure 1. RGB composites of the five HS^3 regions. The [C II] (green) and [O I] (blue) are on the same intensity scale from 0 to 3×10^{-7} W m^{-2} sr^{-1}, whereas the PACS 160 μm image (red) is shown on a scale from 0 to 2×10^{-5} W m^{-2} sr^{-1}. All images are displayed using a logarithmic stretch. The black contours show MCELS Hα intensity (Smith & MCELS Team 1999) at linear intervals (1, 2, 3, 4, 5, 10, 15 $\times 10^{-14}$ erg cm^{-2} s^{-1}) to show the location of massive star formation throughout the regions, with the region designations based on Hα from Henize (1956) and Davies et al. (1976) indicated. The names of overlapping regions from Rubio et al. (1993a, 1993b, 1996) SEST surveys are listed in parentheses. The orange squares show the coverage of the [O III] observations ([N II] has approximately the same coverage), and the red circles show the area covered by the FTS observations. The black dashed line rectangles show the approximate coverage of the ALMA maps. The two inset spectra, labeled Regions 1 and 2, show spectral extractions from the PACS cube in some of the faintest regions covered by the strips. We clearly detect [C II] emission throughout the faint areas and, somewhat unexpectedly, also [O I] 63 μm. The data used to create this figure are available.

clouds containing O^0 in velocity-resolved observations of [O I] (Poglitsch et al. 1996; Leurini et al. 2015). It is unknown how widespread this phenomenon is in the SMC, where 145 μm observations do not exist and velocity-resolved observations are very limited.

In the Milky Way, heavy [O I] self-absorption is usually accompanied by [C II] absorption (e.g., Leurini et al. 2015). There is no indication of absorption in recent [C II] velocity-resolved profiles (Requena-Torres et al. 2016; R. Herrera-Camus et al. 2017, in preparation) and no clear evidence of

self-absorption in [O I] velocity-resolved profiles (Y. Okada et al. 2017, in preparation) in the star-forming regions N25 (located in the north end of the HS^3 "N22" region), N66, and N88 in the SMC. Given the high radiation fields and low A_V throughout much of the SMC, this suggests that in the SMC there is a dearth of high-A_V cold material that may absorb [O I] along the line of sight, while absorption contamination is likely more common in the Milky Way (e.g., Leurini et al. 2015). As mentioned above, another indicator of optical depth or absorption in the [O I] 63 μm line is anomalously high [O I]
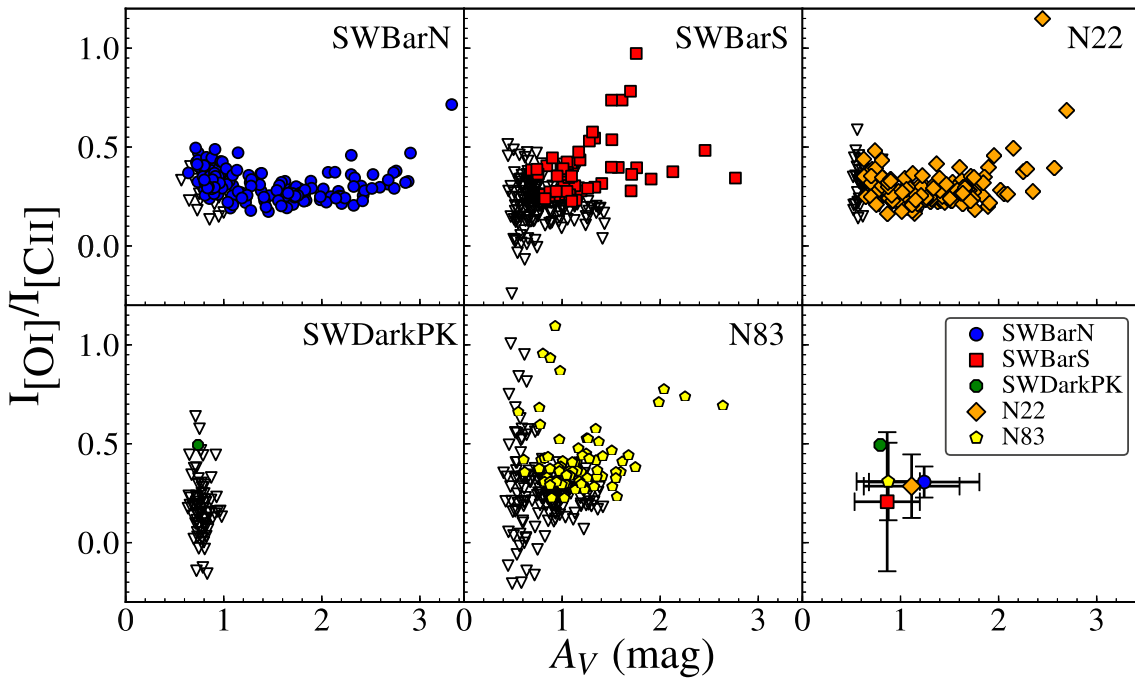
Figure 2. Ratio of the integrated intensity of [O I] to that of [C II] as a function of A_V for the HS³ regions. The colored symbols show independent measurements detected at $>3\sigma$ in both [O I] and [C II], with the downward-pointing triangles indicating upper limits (where $I_{O I} < 3\sigma$). The bottom right panel shows the average values, with the error bars showing 1σ on mean for each of the regions except for SWDarkPK, for which we show the one measurement $>3\sigma$. The mean line ratios were calculated to include the upper limits ("left-censored" data) using the cenfit routine in the R package NADA (Helsel 2005; Lee 2017). The [O I]/[C II] ratio is mostly constant across the regions, independent of A_V, and has a typical value of ~0.3.

145 μm/63 μm ratios (Stacey et al. 1983). While there are no *Herschel* PACS observations of [O I] 145 μm in the SMC, in the LMC three regions were observed in [O I] 145 μm to 63 μm by Cormier et al. (2015) and in 30 Doradus by Chevance et al. (2016). Only two of these regions, N159 (the site of the brightest CO emission in the LMC; Israel et al. 1993) and 30 Doradus (one of the most active star-forming regions in the Local Group), have high 145 μm/63 μm ratios, with a ratio of 0.11 found in N159 and >0.1 in 30 Doradus, which is not much higher than the theoretical limit of 0.1 for the expected ratio for optically thin emission for $T > 300$ K (Tielens & Hollenbach 1985). If the line were self-absorbed in our observations, we would expect to see lower [O I]/[C II] ratios in high-density regions at higher A_V, but we see the opposite. We conclude that it is unlikely that the [O I] 63 μm line is significantly affected by absorption in our SMC observations.

3.1.2. [O I]-to-[C II] Ratio

What is the origin of the observed [C II] emission? Figure 2 shows the integrated intensity ratio of [O I] to [C II]. The observed ratio is approximately constant, with a value of [O I]/[C II] ~ 0.3. One of the main departures from the mostly flat trend in [O I]/[C II] with A_V is a cluster of higher ratio values in the SWBarS, which are found in the H II region N13, indicating the presence of warm, dense gas. This is also the typical value observed in the disks of the KINGFISH sample of nearby galaxies (Herrera-Camus et al. 2015). Using the [C II] and [O I] cooling curves calculated for diffuse gas under SMC conditions (M. Wolfire et al. 2017, in preparation), a ratio [O I]/[C II] ~ 0.3 is indicative of densities of $\sim10^2$–10^3 cm^{-3}, which are consistent with dense cold neutral medium (CNM) and/or molecular gas. Figure 3 shows the similarity between the mid-infrared H_2 S(0) quadrupole rotational line at 28.8 μm and the

[C II] emission. This clearly demonstrates that molecular gas is associated with the [C II]-emitting material, strongly suggesting that most of the [C II] emission in our mapped regions has a PDR origin and arises from the surfaces of molecular clouds.

3.1.3. Photoelectric Heating Efficiency at Low Metallicity

The dominant heating source is the photoelectric effect where a dust grain absorbs an FUV photon and ejects an electron that heats the gas through collisions. The [C II] and [O I] FIR line emission dominates the cooling of the diffuse atomic and molecular gas, as well as PDRs. By combining the [C II] and [O I] line emission, we can account for most of the gas cooling that is attributed to gas heated by the photoelectric effect. Taking the ratio of [C II] and [O I] intensities to the TIR intensity indicates the fraction of the power absorbed by the grains that goes into heating the gas through the photoelectric effect. Figure 4 shows the mean [C II]+[O I]/TIR ratios for each of the HS³ regions as a function of the mean dust temperature from Lee et al. (2015). The ratio of [C II]+[O I]/TIR ranges from ~0.01 to 0.018 in the SMC. This is similar to the LMC, where Rubin et al. (2009) find that the [C II] in emission from BICE observations accounts for $\sim1\%$ of the TIR emission. These ratios are on the high end of the range observed for the Milky Way and galactic nuclei of 0.1%–1% using KAO observations (Stacey et al. 1991), $<0.1\%$–1% for the nearby KINGFISH galaxies using *Herschel* observations (Smith et al. 2017), normal galaxies using *ISO* observations (Malhotra et al. 2001), and M31 using *Herschel* observations (Kapala et al. 2015). We also see a trend of decreasing ratios with high dust temperatures, also observed by Malhotra et al. (2001), Croxall et al. (2012), and Kapala et al. (2015), which is commonly attributed to the increased grain charging at warmer dust temperatures that increases the energy threshold for the
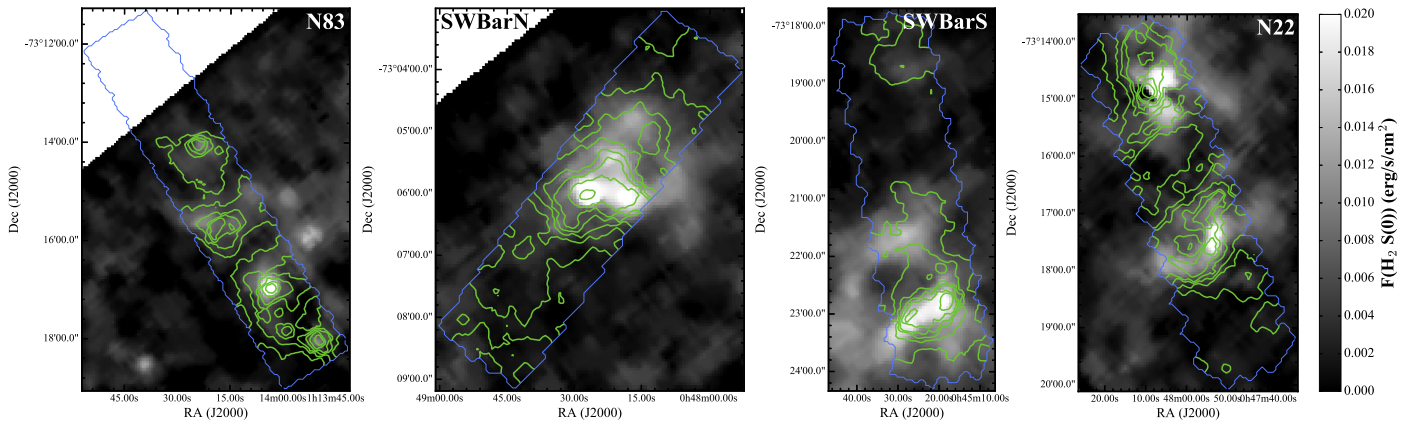
Figure 3. Images of the H_2 S(0) 28.2 μm line from S^4MC (Sandstrom et al. 2012) resampled to match the HS^3 [C II] images. Contours show the [C II] integrated intensity at levels of 0.3, 0.5, 0.7, 0.9, 1.2, 1.5, 2.0, 3.0 $\times$ 10^{-7} W m^{-2} sr^{-1}, with the blue line showing the [C II] map coverage. The excellent correspondence between the structures provides evidence that [C II] is tracing the molecular gas in the PDRs.
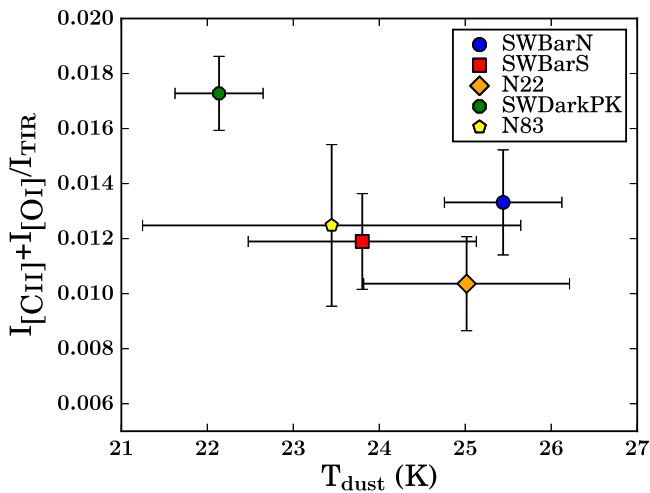

Figure 4. Mean ratios of the [C II] and [O I] intensities to the TIR, an indicator of the photoelectric heating efficiency, as a function of mean dust temperature (T_{dust}) from Lee et al. (2015). The error bars show 1σ on the mean.

photoelectric effect ejection of electrons and decreases the energy, and therefore the amount of gas heating, per ejected electron.

3.2. [N II] and Contribution from Ionized Gas

The HS^3 data set includes sparsely sampled FTS spectra for the SWBarN, SWBarS, N22, and N83 regions, as well as a pointing toward the most active star-forming region in the SMC, the giant H II region N66. In Figure 5 we show the long-wavelength array (SLW) spectra in red and the short-wavelength array (SSL) in blue, with the positions of the ^{12}CO, [C I], and [N II] lines indicated. We see clear detections of the lower rotational transitions of ^{12}CO and the [N II] 205 μm lines, as well as weak detections of [C I].

We do not detect the [N II] 122 μm line in any of the regions, whereas the [N II] 205 μm line is detected in all regions in the FTS spectra (see Figure 5). Because the ionization potential of nitrogen of 14.5 eV is higher than that of hydrogen, ionized nitrogen traces the ionized gas. The [N II] 122 and 205 μm lines result from the fine-structure splitting of the ground state of ionized nitrogen and are primarily excited by collisions with electrons.

The critical densities of the 122 and 205 μm lines differ, and the ratio can be used to estimate the electron density (n_e). The [N II] 122 μm line has a higher critical density for collisions with electrons ($n_e \sim 300$ cm^{-3}) compared to the 205 μm line ($n_e \sim 40$ cm^{-3}), which has a critical density similar to that for exciting the [C II] 158 μm line with collisions with electrons. Thus the ratio of [C II]/[N II] 205 μm in ionized gas is independent of density, and it depends only on the relative abundances of the ions, which are likely similar to the elemental abundances.

The sensitivity of the [N II] 122 μm observations is $\sim 3 \times 10^{-10}$ W m^{-2} sr^{-1}, while the range of detected [N II] 205 μm intensities is $\sim(2-5) \times 10^{-10}$ W m^{-2} sr^{-1}. Based on these measurements, the [N II] 122 μm/205 μm ratio is $\lesssim 1$ in regions where the [N II] 205 μm line is detected. Using the electron collision strengths from Tayal (2011), this translates to an upper limit to the electron density of $n_e \lesssim 20$ cm^{-3} since this is approximately the [N II] 122 μm/205 μm ratio diagnostic lower density limit. In other words, our measurements are consistent with a relatively low density for the ionized material, somewhat lower than the mean ionized gas density observed in the KINGFISH sample of galaxy disks of $n_e \sim 30$ cm^{-3} (Herrera-Camus et al. 2016).

In Figure 6, we show the [N II] 205 μm/[C II] ratio for all of the pointings where [N II] 205 μm is detected at $>3\sigma$ and where the [C II] intensity is found for the central FTS bolometer position after convolving the map to the FTS resolution ($\sim 17''$). We see that the [N II] 205 μm emission ranges from 0.2% to 1.2% of the [C II] emission. For carbon emission arising from ionized gas with a ratio $C^+/N^+ \approx C/N$ similar to Galactic we would expect [N II] 205 μm/[C II] ~ 0.2, mostly independent of density owing to the similarity in the critical densities (Tayal 2008, 2011). Because the [N II] emission can only arise from ionized gas, the fact that we measure over ~ 20 times fainter [N II] relative to [C II] suggests that the contribution of ionized gas to [C II] is at most 5%.

These ratios represent the maximum ratios throughout the regions since the FTS observations targeted the bright CO emission, which tends to be near H II regions, and as such will have the highest fraction of [C II] emission arising from ionized gas. The observed [N II] 205 μm/[C II] ratios are lower than the typical values found in the KINGFISH survey of 0.057 (Croxall et al. 2017). Similarly, Cormier et al. (2015) find depressed [N II] 122 μm/[C II] in dwarf galaxies, suggesting
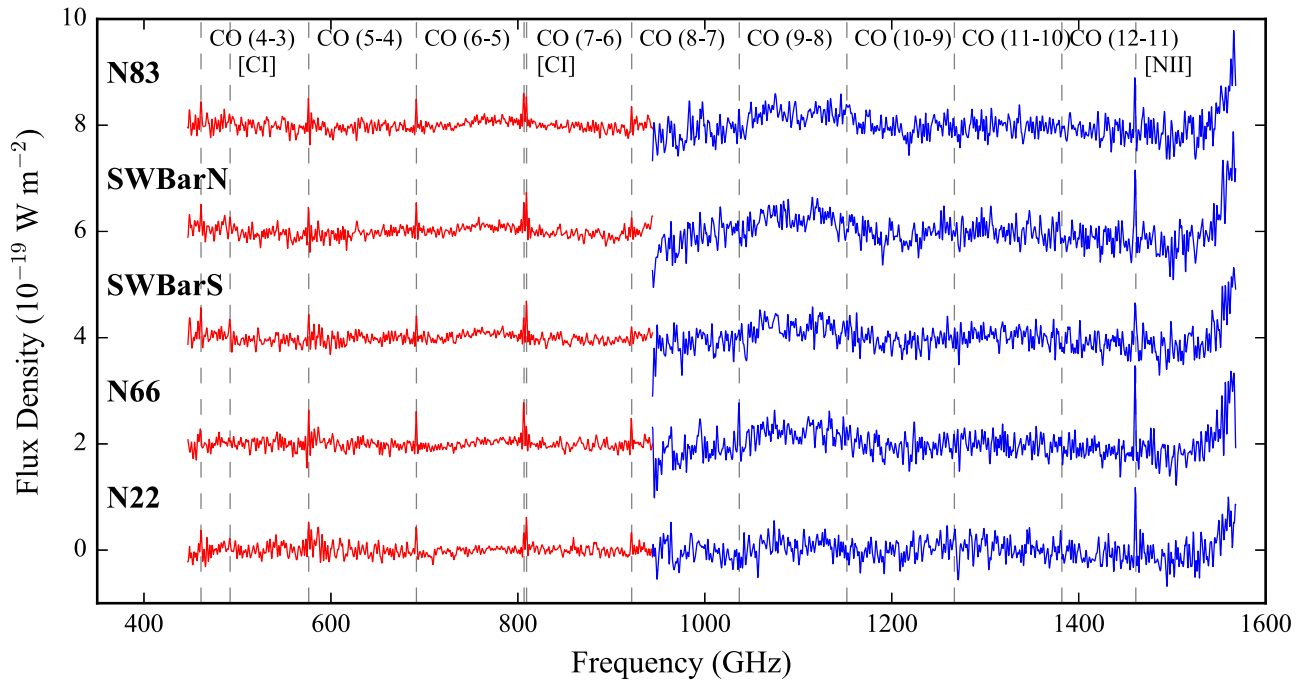
Figure 5. FTS SLW (red) and SSW (blue) spectra averaged over all the bolometers for HS^3 regions SWBarN, SWBarS, N22, and N83, plus N66 (the target of PACS observations from the *Herschel* GTKP SHINING project), with each spectrum being offset by 2×10^{-19} W m^{-2} sr^{-1}. The SLW and SSW spectra have a second-order polynomial fit and are subtracted to remove the baseline. The gray dashed lines indicate the positions of possible spectral lines. There are no detections of the CO ladder in the SSW except for CO (9–8) in N66, which also displays CO (8–7) in the SLW, showing that gas associated with the molecular complex in this giant H II region is warm and highly excited.
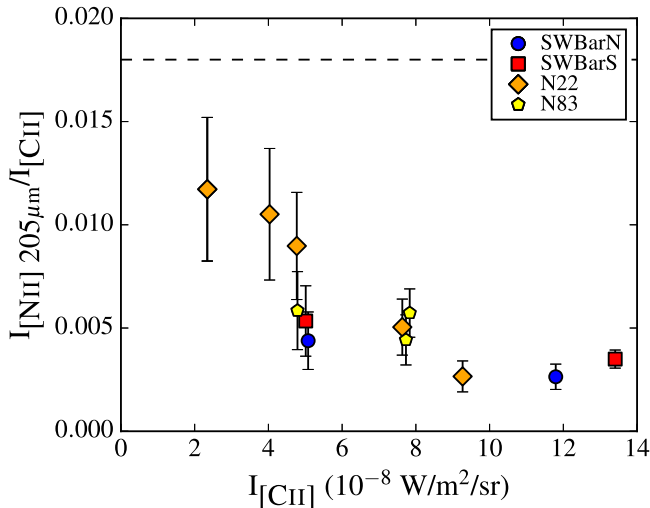
Figure 6. Ratio of integrated intensities of [N II] 205 μm ($I_{\text{[N II]}}$ 205 μm) to [C II] ($I_{\text{[C II]}}$) as a function of the [C II] intensity for FTS bolometer measurement of [N II] 205 μm, which is $>3\sigma$ for each of the regions. The error bars show the 1σ uncertainty on the line ratio, which is dominated by the uncertainty in the [N II] 205 μm flux (the uncertainty in $I_{\text{[C II]}}$ is smaller than the symbols). The FTS pointings for each of the regions targeted the star-forming peak, which tends to coincide with the peak CO emission. The ratios are low and naturally peak toward higher values at lower [C II] intensities. The black dashed line shows the lowest observed ratio of [N II] 205 μm/[C II] ~ 0.018 in the KINGFISH sample (Croxall et al. 2017).

that ionized gas only produces a small fraction of the [C II] emission in low-metallicity environments.

3.3. [O III] and Highly Ionized Material

The [O III] 88 μm line traces ionized gas, as the second ionization potential of oxygen is ~ 35 eV, much higher than
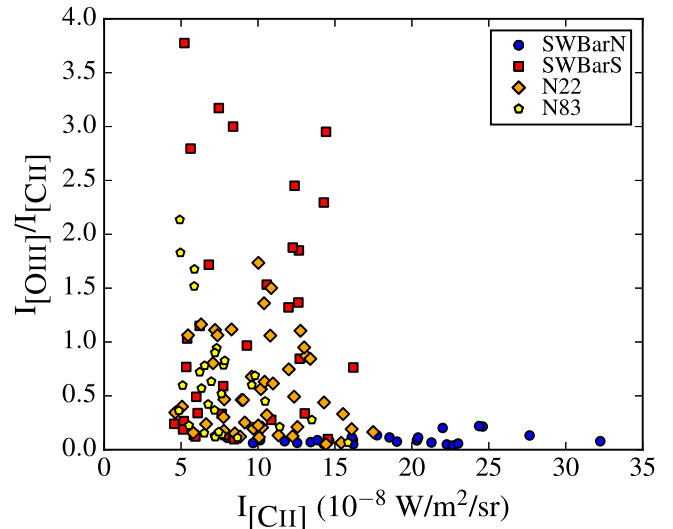
Figure 7. Ratio of integrated intensities of [O III] 88 μm ($I_{\text{[O III]}}$) to [C II] ($I_{\text{[C II]}}$) as a function of the [C II] intensity, where [O III] is detected at $>3\sigma$ for each of the regions. The [O III] maps cover the main H II regions in the HS^3 regions. We see high $I_{\text{[O III]}}/I_{\text{[C II]}}$ ratios in all of the regions except SWBarN, where there is no large H II region and likely less ionized gas.

hydrogen. H^{3}S obtained [O III] observations toward the dominant H II region in each strip. We observed bright [O III] emission from all of these pointings. Van Loon et al. (2010) also detected [O III] toward a subset of their sample of compact sources in the SMC using *ISO* spectra. Figure 7 shows the [O III]/[C II] ratios for the SMC regions, which reach as high as [O III]/[C II] ~ 4. Observations of the [O III]/[C II] ratio for higher-metallicity galaxies based on *ISO* data presented by Brauher et al. (2008) found lower ratios in the range of [O III]/[C II] ~ 0.1–1.5. The higher values in the SMC are similar to

the ratios found for dwarf galaxies observed with *Herschel* PACS as part of the DGS with a median and range of $[\text{O\,{\sc iii}}]/[\text{C\,{\sc ii}}] = 2.0^{+13.0}_{-0.52}$ (Cormier et al. 2015). These comparisons to measurements in other galaxies should be tempered somewhat by the fact that the SMC observations are pointings toward H II regions obtained at high spatial resolution, while the comparison work typically samples larger scales and therefore a mix of ionized and neutral material.

While the critical density for the [N II] 122 μm line is similar to that for [O III], the [O III] ionization potential is much higher, as is the energy above ground for excitation. Cormier et al. (2015) suggest that the hard radiation fields found at lower metallicity in dwarf galaxies could explain the high [O III] emission and high [O III]-to-[N II] 122 μm ratios, with a median ratio of 86 found for the DGS sample. Note that we failed to detect [N II] 122 μm emission toward these same pointings. A combination of hard radiation fields and low-density ionized gas may explain the high [O III]-to-[N II] 122 μm ratios present in the SMC, with the the a lower limit of [O III]/[N II] 122 μm $\sim$ 25 (calculated using 3σ of the [O III] intensity and the 1σ sensitivity of the [N II] intensity). We note that the O/N abundance ratio in the SMC is similar to that found in the solar neighborhood (Russell & Dopita 1992), and it is unlikely that a difference in abundance ratios would explain the relatively high [O III] emission. Understanding the ISM conditions that produce the [O III] line emission in low-metallicity environments is critical for interpreting new and future observations of FIR cooling lines in high-redshift galaxies using ALMA (e.g., Inoue et al. 2016).

3.4. High-resolution Molecular Gas: ^{12}CO and ^{13}CO

We mapped and detected ^{12}CO and ^{13}CO $(2-1)$ in all of the regions targeted by ALMA, shown in Figure 8. Table 5 summarizes the properties of the detected CO and the sensitivities of the integrated intensity maps. We do not detect C^{18}O with our current observations, which had the minimum integration time allowed per pointing to increase the coverage of the mosaics. Despite the lower metallicity and less dust shielding, ^{12}CO and ^{13}CO form and emit brightly in small clumps. Our high-resolution ALMA ACA data show that the bright CO emission is found in small structures, which we will quantify in a forthcoming paper (K. Jameson et al. 2017, in preparation), which were unresolved by previous observations. The clumpy nature of the CO emission at low metallicity has also been observed in the N83C star-forming region in the wing of the SMC (Muraoka et al. 2017), in the dwarf galaxies WLM (Rubio et al. 2015) and NGC 6822 (Schruba et al. 2017), and in 30 Doradus of the LMC (Indebetouw et al. 2013).

For most of the regions, a large fraction of the flux is recovered by the high-resolution ACA maps. In the SWBarS and SWBarN regions, the ACA flux represents $\sim$60% of the flux in the combined ACA+TP ^{12}CO maps. In SWDarkPK, nearly 100% of the flux is from the high-resolution imaging, whereas in the N22 region most of the emission is diffuse, with only $\sim$30% of the flux found at high resolution. The higher fraction of diffuse ^{12}CO emission in N22, less in SWBarS and SWBarN, and none in SWDarkPK are likely due to their varying evolutionary stages: N22 is the most evolved region, with multiple large H II regions around the CO emission; SWBarS and SWBarN both are actively forming stars and have one prominent H II region; and SWDarkPK has no signs of active star formation. The higher UV fields likely increase how

deep the PDR extends into the molecular cloud and the amount of diffuse CO emission associated with the PDR. In the more evolved regions (particularly N22), the densest peaks of molecular gas may have already been dispersed by star formation, leaving less clumps of molecular gas and increasing the fraction of diffuse CO emission.

Figure 9 shows the comparison between the ^{12}CO and ^{13}CO $(2-1)$ emission. We find average ^{12}CO/^{13}CO $(2-1)$ ratios of $\sim$5–7.5 (in units of K km s^{-1}). These ratios are consistent with previous measurements in the SMC toward emission peaks (Israel et al. 2003) and in nearby galaxies (e.g., Paglione et al. 2001; Krips et al. 2010). In the Milky Way the ratios are similar to what we obtain for the SMC, with an average of $\sim$5 (Solomon et al. 1979) in the inner Galaxy and somewhat higher ratios of $\sim$7 for large parts of the plane (Polk et al. 1988) and in the outer Galaxy clouds (Brand & Wouterloot 1995).

3.5. Estimating the Optical Depth of ^{12}CO

The linear trend with no turnover observed between ^{12}CO and ^{13}CO indicates that while the ^{12}CO $(2-1)$ transition is optically thick where there is ^{13}CO, ^{13}CO likely remains optically thin for these observations. The ^{13}CO-to-^{12}CO ratio gives the optical depth of ^{13}CO $(2-1)$, and from that we can estimate the optical depth of the ^{12}CO $(2-1)$ emission. The Rayleigh–Jeans radiation temperature of the CO line emission is

$$T_R = J_R(T_{\text{ex}})(1 - e^{-\tau}), \qquad (2)$$

where T_{ex} is the excitation temperature and τ is the optical depth of the line. The observed intensity is

$$J_R(T_{\text{ex}}) = \frac{h\nu}{k}\left(\frac{1}{e^{(h\nu/kT_{\text{ex}})} - 1} - \frac{1}{e^{(h\nu/kT_{\text{bg}})} - 1}\right), \qquad (3)$$

where T_{bg} is the background temperature (taken to be the cosmic microwave background of 2.73 K). If we assume that both lines share the same excitation temperature, then the ratio of the line brightness temperatures for the two isotopic species can be used to estimate the optical depth of the more abundant species. This is strictly correct only in the high-density regime ($n \gg n_{\text{cr}}$, where $n_{\text{cr}} \sim 10^4$ cm^{-3} is the critical density of the ^{13}CO $2-1$ transition that is assumed to be optically thin), where the level populations will follow a Boltzmann distribution at the kinetic temperature of the gas. For ^{12}CO and ^{13}CO $(2-1)$,

$$\frac{T_{R,^{12}\text{CO}(2-1)}}{T_{R,^{13}\text{CO}(2-1)}} = \frac{1 - e^{-\tau_{^{12}\text{CO}}}}{1 - e^{-\tau_{^{12}\text{CO}}/X}}, \qquad (4)$$

where X is the abundance ratio of ^{12}CO/^{13}CO. Assuming that $\tau_{^{12}\text{CO}} \gg 1$, we can solve for the optical depth of ^{12}CO:

$$\tau_{^{12}\text{CO}} = -X \ln(1 - T_{R,^{13}\text{CO}(2-1)}/T_{R,^{12}\text{CO}(2-1)}). \qquad (5)$$

We adopt an abundance ratio of $X = 70$, which is appropriate for the Milky Way (Wilson & Rood 1994), since it is intermediate between the two values found in the SMC using radiative transfer modeling of the ^{12}CO and ^{13}CO lines from Nikolić et al. (2007). Using this isotopic abundance ratio, the average ^{12}CO/^{13}CO values (where $I_{^{13}\text{CO}} > 3\sigma$) indicate optical depths of $\tau_{^{12}\text{CO}} = 7.8, 13.8, 12.5,$ and 19.0 for the SWBarN, SWBarS, N22, and SWDarkPK regions, respectively. In practice, ^{12}CO is likely to be more highly excited than ^{13}CO
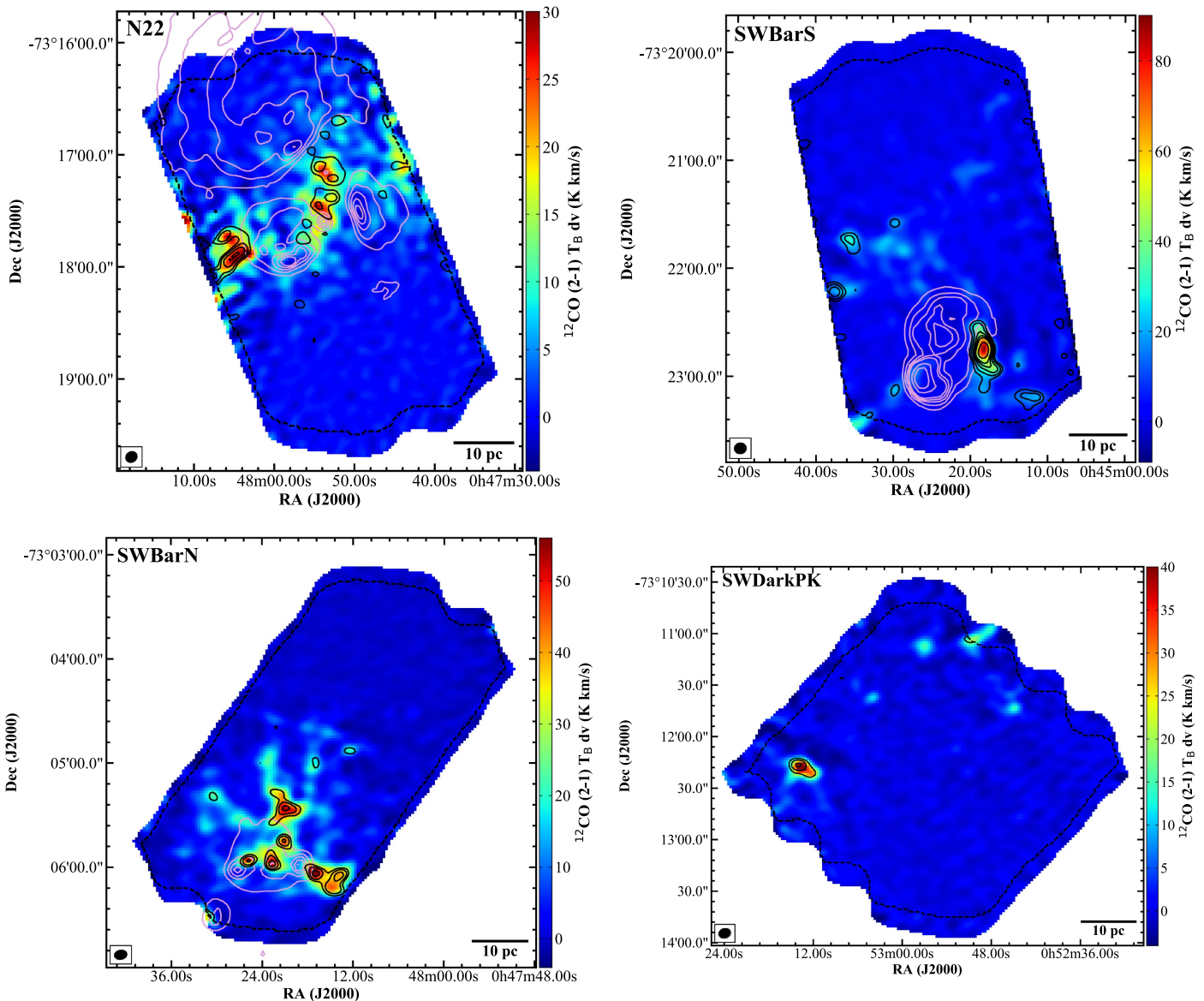
Figure 8. Integrated intensity maps of ALMA ACA+TP ^{12}CO $(2-1)$, with black contours showing ALMA ACA ^{13}CO $(2-1)$ at levels of 2.5, 4, 6, 8, 10, 15 K km s^{-1} and the light-purple contours showing the Hα contours shown in Figure 1. The black dashed line shows the coverage of the ^{13}CO $(2-1)$ image. The sensitivities of the maps are listed in Table 5. The data used to create this figure are available.

owing to radiative trapping, which would result in smaller ^{13}CO/^{12}CO ratios and somewhat underestimate the optical depth by this method. At these size scales ($\sim$2 pc), the beam may include high- and low-density gas, with the low-density gas more likely to have more excited ^{12}CO and also to decrease the ^{13}CO/^{12}CO ratio. However, the density in the [C II]-emitting gas (see Section 4.3.2 and Figure 14) is already high, and there is unlikely to be a strong contribution from ^{12}CO-emitting low-density gas.

3.6. Estimating X_{CO} Using ^{13}CO

The ^{12}CO emission is likely to be optically thick under most conditions found in a molecular cloud, and indeed we estimate high average optical depths of the ^{12}CO $(2-1)$ line emission. Assuming, however, that ^{13}CO is optically thin is reasonable throughout much of a cloud, given the high isotopic ratio and

the lower C abundance in the SMC. We can then use the ^{13}CO intensity to estimate a molecular gas column density and from that infer a ^{12}CO-to-H$_2$ conversion factor (X_{CO}).

We use Equations (2) and (3) and the assumption that the excitation temperature is the same for both the ^{12}CO and ^{13}CO emission to calculate the optical depth of the ^{13}CO emission. The total column density of ^{13}CO ($N_{13_{CO}}$) as a function of the excitation temperature (T_{ex}) and optical depth of ^{13}CO ($\tau_{13_{CO}}$) for the $J = 2 \rightarrow 1$ transition is given by (Garden et al. 1991; Bourke et al. 1997)

$$N_{13_{CO}} = 1.12 \times 10^{14} \frac{(T_{ex} + 0.88)e^{5.29/T_{ex}} \int \tau_{13_{CO}} dv}{1 - e^{-10.6/T_{ex}}}. \qquad (6)$$

We then make the approximation that the integral of $\tau_{13_{CO}}$ is taken to be the line center optical depth ($\tau_{13_{CO,0}}$) multiplied by the ^{13}CO FWHM ($\Delta v_{13_{CO}}$) (Dickman 1978). To convert from

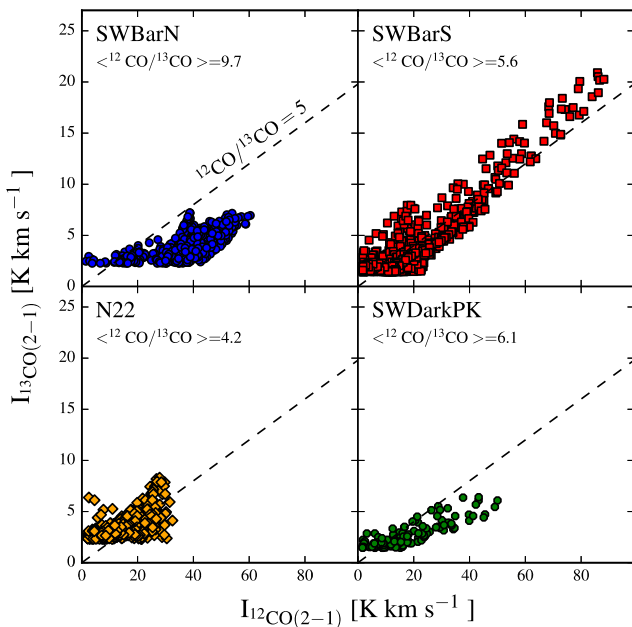**Figure 9.** Ratio of integrated intensity of ^{12}CO $(2-1)$ to ^{13}CO, where both are detected at $>3\sigma$. The average ^{12}CO/^{13}CO ($\langle^{12}$CO/^{13}CO$\rangle$) are listed for each region. The dashed line shows a typical ratio found in the Milky Way of ^{12}CO/^{13}CO = 5.

$N_{^{13}CO}$ to N_{H_2}, we scale by the ^{12}CO/^{13}CO abundance of 70 (Nikolić et al. 2007) and the ^{12}C/H abundance of 2.8×10^{-5} (for a justification see Section 4). This results in $H_2/^{13}$CO $= 1.25 \times 10^{6}$.

Figure 10 shows the distribution of X_{CO} for lines of sight with $I_{^{13}CO} > 3\sigma$ and $A_V > 1$, where we expect the molecular gas to be primarily traced by ^{12}CO emission. We estimate the $A_V > 1$ by converting $N_{^{13}CO}$ to A_V using the empirically determined relationship $A_V \approx 4 \times 10^{-16} N_{^{13}CO}$ cm mag^{-1} from Dickman (1978) for Milky Way dark clouds, which should be appropriate if the ^{13}CO abundance scales the same as the dust abundance. The distributions have median values of $(1.3-2.3) \times 10^{20}$ cm^{-2} (K km s^{-1})$^{-1}$, which are consistent with a Milky Way X_{CO}.

Estimating X_{CO} using ^{13}CO involves a number of assumptions that are not well constrained. We assume that the ^{13}CO and ^{12}CO lines share the same excitation temperature, that this temperature can be inferred from the brightness of the ^{12}CO emission at our spatial resolution (typically $\sim$2.3 pc; see Table 4), and that the gas is in LTE. We do not account for potential beam dilution, which could decrease our measurements of T_{ex} from ^{12}CO and cause us to overestimate $\tau_{^{13}CO}$ and $N_{^{13}CO}$ and overestimate X_{CO}. Wong et al. (2017) make similar estimates of the molecular gas mass using ^{12}CO and ^{13}CO ALMA observations of molecular clouds in the LMC, which suffer from similar uncertainties, and find evidence that their N_{H_2} estimates were biased toward higher values. Conversely, the assumption of LTE could potentially cause $N_{^{13}CO}$ to be underestimated by a factor of $\sim$1.3–2.5 based on the comparison to simulations of molecular clouds by Padoan et al. (2000) for the typical $N_{^{13}CO}$ in our regions ($\sim 10^{15}$ cm^{-2}). Both the ^{12}CO/^{13}CO and ^{12}C/H, which we assume also traces ^{12}CO/H, are uncertain in the SMC. The existing ^{12}C/H measurements vary by $\pm$30%. Nikolić et al. (2007) constrain
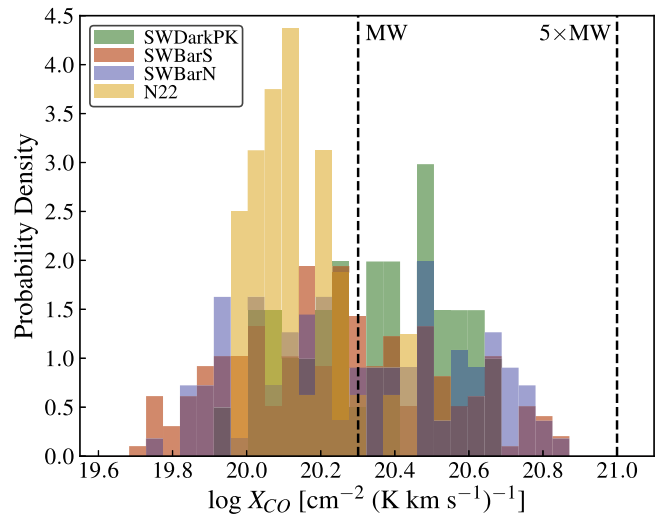

Figure 10. Histogram of the probability density of X_{CO} for areas in each region with $I_{^{13}CO} > 3\sigma$ and at $A_V > 1$ with N_{H_2} estimated using ^{13}CO. The vertical dashed black line shows the Galactic value of $X_{CO} = 2 \times 10^{20}$ cm^{-2} (K km s^{-1})$^{-1}$ and five times the Galactic value. We see that our estimates of X_{CO} in the high-A_V regions peak close to the Galactic value.

Table 5
ALMA CO Properties

Region	Δv_{LSR} (km s^{-1})	T_{peak}[a] (K)		Map Sensitivity[b] (K km s^{-1})		
		^{12}CO	^{13}CO	^{12}CO	^{13}CO	C^{18}O
SWBarS	104–133	18.6	4.9	2.1	1.7	1.2
N22	113–133	15.9	2.6	2.1	2.4	1.0
SWBarN	104–140	14.6	4.3	1.8	2.2	1.2
SWDarkPK	137–160	12.1	3.0	1.9	1.8	1.3

Notes.
[a] In 0.3 km s^{-1} channels.
[b] Defined as $3 \times$ rms in regions away from line emission.

the ^{12}CO/^{13}CO abundance ratio to $\pm\sim$30%, but recent radiative transfer modeling by Requena-Torres et al. (2016) finds ^{12}CO/^{13}CO $=$ 50, which is at the lower end of the range found by Nikolić et al. (2007). If we are overestimating the abundance of ^{13}CO, which could be by up to a factor of 2 based on the metallicity scaling of the Milky Way measurement of $H_2/^{13}$CO from Dickman (1978), then we would also underestimate X_{CO} by the same amount. It is unclear how all of these uncertainties would balance out in these specific regions. Ultimately, the data are consistent with a conversion factor similar to that of the Milky Way, but we caution the reader that there is a large degree of uncertainty on this estimate.

3.7. Relationship between ^{12}CO and [C II]

[C II] emission can arise from neutral atomic gas, molecular gas, and ionized gas. Our comparison of [C II] to [N II] shows that only a small fraction of the [C II] emission arises from ionized gas. While [C II] emission is an important coolant of the CNM (Dalgarno & Black 1976; we explore this further in Section 4.2), PDRs are expected to produce bright [C II] emission (Hollenbach & Tielens 1999, and references therein). The carbon will exist as CO in the dense parts of the molecular gas, but at the edges of the cloud the lack of shielding will dissociate CO and much of the carbon will exist as C$^+$, while
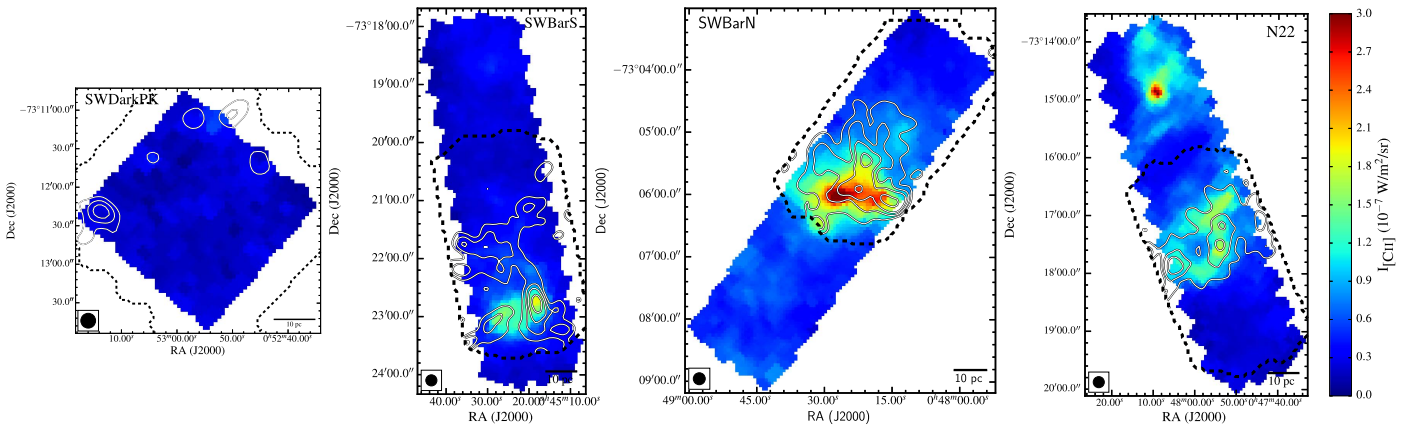
Figure 11. Maps of the [C II] integrated intensity, with black contours showing the integrated intensity of the ALMA ACA+TP ^{12}CO $(2-1)$ map convolved to the [C II] resolution ($\theta = 12''$) at levels of 0.3, 1, 2, 4, 6 × 10^{-10} W m^{-2} sr^{-1} (2, 8, 16, 32, 48 K km s^{-1}). The dashed black lines show the coverage of the ACA maps. There is generally good agreement between the peaks in the [C II] and ^{12}CO emission, and the faint [C II] emission tends to trace the faint ^{12}CO structure, strongly suggesting that most of the [C II] is originating from PDRs and is associated with molecular gas.

there can still be molecular (H$_2$) gas (e.g., Israel et al. 1996; Bolatto et al. 1999; Wolfire et al. 2010). This leads to a layer of molecular gas surrounding the molecular cloud associated with [C II] but no ^{12}CO emission. Studying the ^{12}CO-to-[C II] ratio can determine whether the [C II] emission is primarily associated with the PDR and provide insight into the structure of the molecular cloud and its associated faint CO gas.

What is the origin of the [C II] emission in our SMC regions? Figure 11 shows the [C II] integrated intensity maps, with the ALMA ^{12}CO $(2-1)$ integrated intensity shown with contours. There is a striking similarity between the structures, at both high and low intensity, but the [C II] extends throughout the mapped region, whereas the CO emission is more localized. The similarity in integrated intensity emission structure suggests that the [C II] emission predominantly traces the molecular gas. This is reinforced by the velocity-resolved observations. Recent observations of the [C II] 158 μm line using the GREAT instrument on SOFIA for individual pointings throughout some of the HS^3 regions show that the velocity ranges covered by the [C II] and ^{12}CO $(2-1)$ emission are similar, although in an FWHM sense the [C II] line can be up to ∼50% wider than the ^{12}CO line (R. Herrera-Camus et al. 2017, in preparation). Other SOFIA GREAT observations of SMC star-forming regions N66, N25/26 (covered in the HS^3 "N22" region), and N88 show that the [C II] profile is similar to the ^{12}CO profile, with the [C II] profile being up to ∼50% wider (Requena-Torres et al. 2016). SOFIA GREAT observations of [C II] in M101 and NGC 6946 also show that the velocity profile of [C II] has a better correspondence with ^{12}CO than H I (de Blok et al. 2016). We show one example GREAT [C II] spectrum for one pointing in the SWBarN region compared with the beam-matched ALMA ^{12}CO $(2-1)$ profile and the H I emission (at a resolution ∼$1'$) toward the same point in Figure 12. As mentioned above, the CO and [C II] cover a very similar velocity range, which is much more restricted than that of the H I emission. This strongly suggests that toward these molecular regions [C II] is dominated by emission arising from molecular gas rather than atomic gas.

Furthermore, there is a clear similarity between the [C II] map and the map of the H$_2$ rotational line emission at 28.2 μm (see Figure 3). This line requires warm gas ($T \gtrsim 100$ K) to be excited, so it is a poor tracer of the bulk of the molecular mass.
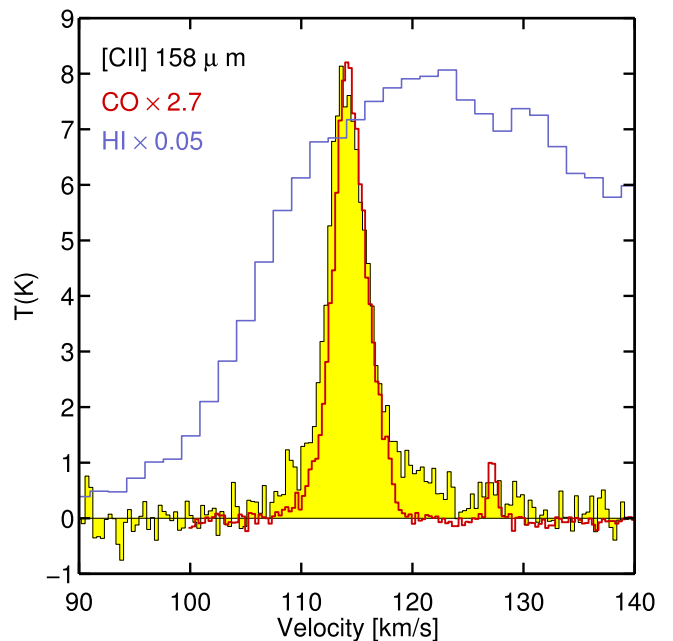

Figure 12. Spectrum of [C II] from one pointing observed with SOFIA GREAT (R. Herrera-Camus et al. 2017, in preparation; region R8), with the yellow filled histogram showing the data in 0.3 km s^{-1} bins, with scaled spectra of the ALMA ^{12}CO $(2-1)$ in red and H I in purple for the same area in the SWBarN region with velocity in the LSRK reference frame. This illustrates that the velocity profile of the [C II] emission is most similar to the ^{12}CO and not the H I, suggesting that a significant fraction of the emission comes from molecular gas. It also shows that the [C II] emission profile can have more extended wings at low or no ^{12}CO intensity, in this case by 5–10 km s^{-1}, which makes the total extent of the [C II] profile wider (by at most ∼50%) than the ^{12}CO line profile.

But the spatial coincidence between these two transitions, together with the [C II]–^{12}CO agreement above, provides strong evidence that a majority of the [C II] emission arises from molecular gas.

3.8. ^{12}CO-to-[C II] Ratio

In Figure 13 we show the ratio of ^{12}CO/[C II] emission as a function of A_V estimated from dust emission (see Section 2.6), which indicates the total column density through the molecular cloud along the line of sight. The ratios are typically much
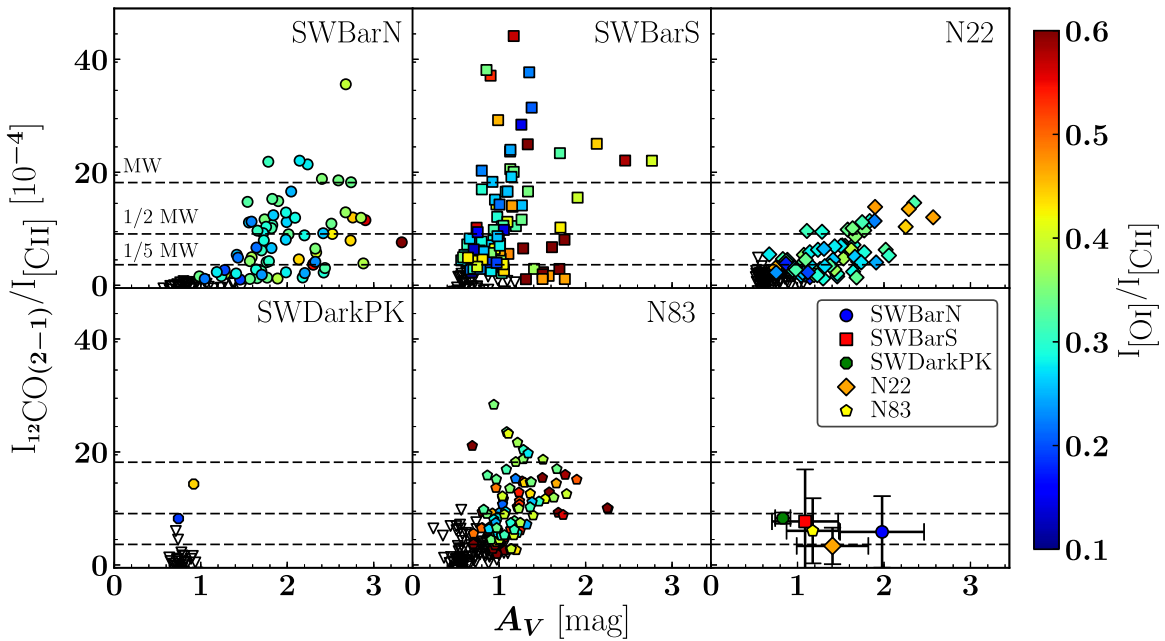
Figure 13. Ratio of the integrated intensity of ALMA ACA+TP ^{12}CO $(2-1)$ to that of [C II] as a function of A_V for the HS^3 regions. The colored symbols show independent measurements detected at $>3\sigma$ in both ^{12}CO and [C II], and the downward-pointing triangles indicate upper limits (where $I_{CO} < 3\sigma$). The overplotted dashed lines show scalings of the canonical [C II]/^{12}CO $(1-0)$ ratio translated to $(2-1)$ assuming thermalized emission for the Milky Way of $\sim 1/4400$ (Stacey et al. 1991). The bottom left panel shows the mean ^{12}CO $(2-1)$/[C II] ratios for each region, which were calculated to include the upper limits ("left-censored" data) using the cenfit routine in the R package NADA (Helsel 2005; Lee 2017). We see a trend of ^{12}CO $(2-1)$/[C II] starting at values much lower than the Milky Way value at low A_V and increasing ^{12}CO $(2-1)$/[C II] toward higher A_V. The [O I]/[C II] ratios also show an increase toward higher A_V, which is consistent with increasing density producing more [O I] emission and/or less [C II].

lower at low A_V and increase with A_V. At higher A_V and deeper within the cloud, there is enough shielding from FUV radiation for significant amounts of ^{12}CO to exist, with an increasing fraction of the carbon in the form of CO as opposed to C or C$^+$. The values of this ratio in the outskirts of the clouds are typically $\sim 1/5$ the fiducial value for the Milky Way of ^{12}CO/[C II] $\sim 1/4400$ (Stacey et al. 1991), which is consistent with the recent global measurements at low metallicity from Accurso et al. (2017). Toward the centers of the clouds, at high A_V, the ratio tends to reach the Milky Way value or higher, as in the case of the SWBarN and SWBarS regions, which show compact, bright peaks in the ^{12}CO and ^{13}CO emission. The lower ^{12}CO-to-[C II] ratios at lower A_V suggest that there is a reservoir of H$_2$ gas that is not traced by bright CO emission.

The low range of A_V in the SWDarkPK region and the high ^{12}CO-to-[C II] values seen at low A_V (e.g., in the SWBarS region) are probably in part due to the geometry of the sources, as well as physical differences in density and radiation field (see Section 4.3.2). Limitations in how we estimate A_V likely also play a role. In order to derive a dust temperature from the dust SED, we need to include the longer-wavelength data, which have poorer resolution. To obtain our A_V estimate, we have thus applied the dust temperature fit on larger ($\sim 40''$) scales, which smooth out any dust temperature variations on small scales, particularly those likely present toward smaller CO clouds or cores. Associated with this, the simple one-dust-temperature modified blackbody fit is also biased toward the higher dust temperatures that will dominate the emission. A high dust temperature results in underestimating τ_{160} and A_V. This combination of inability to resolve small structures and bias toward underestimating A_V should be taken into account when interpreting Figure 13.

4. Estimating H$_2$ Using [C II] and ^{12}CO

At low A_V, in the outer layers of the molecular cloud, the molecular gas will be associated with [C II] emission. As the shielding increases deeper within the cloud at high A_V, the molecular gas will be traced by CO emission. Between the layers traced by [C II] and ^{12}CO, there will be some amount of the molecular gas traced primarily by [C I], but the amount of gas associated with this layer is uncertain. Observationally, existing data suggest that the [C I] traces a small fraction of the total molecular gas in the SMC (Requena-Torres et al. 2016; Pineda et al. 2017). The theoretical work by Nordon & Sternberg (2016) and simulations by Glover et al. (2015) also suggest that most of the neutral carbon will be mixed with the CO, and the amount of molecular gas traced only by [C I] is always much less than that traced by [C II] or CO. Assuming that the amount of gas traced only by [C I] is negligible, we can estimate the total amount of molecular gas by evaluating the [C II] emission coming from H$_2$ gas at low A_V and combining it with the H$_2$ traced by CO emission at high A_V:

$$N_{H_2} = N_{H_2,[C\,II]} + X_{CO}\, I_{CO}. \qquad (7)$$

To convert the [C II] intensity to a column of H$_2$ gas, we have to estimate and remove any possible contribution to the [C II] emission from ionized and atomic gas:

$$I_{[C\,II],mol} = I_{[C\,II]} - I_{[C\,II],ionized} - I_{[C\,II],atomic}, \qquad (8)$$

leaving only [C II] emission arising from molecular hydrogen. This methodology is based on many previous studies that estimate molecular gas based on [C II] emission, with the most recent from Langer et al. (2014) in the Milky Way, Okada et al. (2015) in the LMC, and Requena-Torres et al. (2016) in the SMC. However, those studies relied primarily on [C II], [C I],

Table 6
Properties of H_2 Estimates from [C II]

| Region | Average % $I_{\rm [C\,II]}$ | | $\bar{N}_{\rm H_2, [C\,II]}$ (10^{21} cm^{-2}) | | $M_{\rm H_2, [C\,II]}$ ($10^4\,M_\odot$) | | $M_{\rm H_2, ^{12}CO}$ ($10^4\,M_\odot$) |
	from H I	from H$^+$	Fixed T, n	W16	Fixed T, n	W16	
SWBarS	3%	6%	1.2	0.97	5.05	4.15	1.3
N22	2%	15%	1.6	1.1	5.64	4.13	1.0
SWBarN	2%	7%	2.9	2.5	8.60	7.21	1.7
SWDarkPK	7%	9%	0.48	0.63	0.90	1.16	0.10

and ^{12}CO, lacking any observations that would give them an indication of the temperature and/or density of the [C II]-emitting gas. Our [O I] observations allow us to use the [O I]/[C II] line ratios to constrain the conditions of the [C II]-emitting gas and better estimate the amount of molecular gas.

The integrated [C II] line intensity ($I_{\rm [C\,ii]}$) from collisional excitation assuming optically thin emission is

$$I_{\rm [C\,II]} = 2.3 \times 10^{-24} \left[\frac{2e^{-91.2/T}}{1 + 2e^{-91.2/T} + n_{\rm crit}/n} \right] N_{\rm C^+}, \quad (9)$$

where $I_{\rm [C\,II]}$ is in units of W m^{-2} sr^{-1}, T is the kinetic gas temperature in K, n is the volume density of the collisional partner (H, H$_2$, or e^-) in cm^{-3}, $N_{\rm C^+}$ is the column density of C$^+$ in cm^{-2}, and $n_{\rm crit}$ is the critical density for collisions with a given partner in cm^{-3} (Crawford et al. 1985). We assume a carbon abundance ((C/H)$_{\rm SMC}$) that is the Milky Way abundance scaled by the metallicity of the SMC, such that (C/H)$_{\rm SMC} = Z'_{\rm SMC}$ (C/H)$_{\rm MW} = 2.8 \times 10^{-5}$, taking $Z'_{\rm SMC} =$ 0.2 and (C/H)$_{\rm MW} = 1.4 \times 10^{-4}$ (Sofia et al. 1997), which agrees with the available measurements in the SMC (Kurt et al. 1999; Tchernyshyov et al. 2015).

4.1. $I_{\rm [C\,II]}$ Contribution from Ionized Gas

We estimated a very low contribution to the total [C II] emission from ionized gas based on our [N II] 205 μm measurements (Section 3.2). Here we also estimate the possible contribution using the narrowband Hα data for the SMC to estimate the electron volume density ($n_{\rm e}$) and column density ($N_{\rm e}$) and assuming an ionized gas temperature to calculate $I_{\rm [C\,ii]}$ using Equation (9). The Hα observations provide the emission measure (EM), which can be used to estimate $n_{\rm e}$:

$$\mathrm{EM} = \int n_{\rm e}^2 dl = 2.75 \left(\frac{T}{10^4\,\mathrm{K}} \right)^{0.9} \left(\frac{I_{\rm H\alpha}}{1R} \right) \mathrm{pc\,cm^{-6}}, \quad (10)$$

which we then solve for $n_{\rm e}$ and get

$$n_{\rm e} = \left(\frac{2.75}{l} \left(\frac{T}{10^4\,\mathrm{K}} \right)^{0.9} \left(\frac{I_{\rm H\alpha}}{1R} \right) \right)^{1/2} \mathrm{cm^{-3}}, \quad (11)$$

where $I_{\rm H\alpha}$ is the Hα intensity ($1R = 10^6\,(4\pi)^{-1}$ photons cm^{-2} s^{-1} sr^{-1} = 2.409×10^{-7} erg s^{-1} cm^{-2} sr^{-1} at $\lambda = 6563$ Å), T is the electron temperature, and l is the length over which $n_{\rm e}^2$ is integrated (Reynolds 1991). This procedure is uncertain and known to be biased toward overestimating n_e since the highest densities dominate the EM, but it provides an independent check on the conclusions in Section 3.2, and it also gives us the ability to correct the [C II] maps at higher resolution.

We assume $T_{\rm e} = 8000$ K, appropriate for Galactic H II regions and the warm ionized medium (WIM). While the temperature of H II regions is a strong function of metallicity and is likely higher in the SMC (Kurt & Dufour [1998] measures $T_{\rm e} \approx 12{,}000$ K in N66), Goldsmith et al. (2012) calculate the [C II] critical density for collisions with electrons only up to 8000 K and report $n_{\rm crit,e} = 44$ cm^{-3}. The [C II] emission from ionized gas is not expected to dominate the total [C II] emission (see Section 3.2), so the effect of assuming a lower temperature will be minimal. The most uncertain quantities are the assumed lengths: the distance l over which $n_{\rm e}^2$ is integrated, and the distance used to convert the volume density to a column density. For simplicity, we assume both to be 20 pc, which is approximately the diameter of the largest H II region (N22) found within the survey regions and likely to be the size scale that produces the majority of the measured integrated $n_{\rm e}^2$. The $n_{\rm e}$ we estimate from the Hα emission is $\sim$20–25 cm^{-3}, which is consistent with the upper limit on $n_{\rm e}$ determined from the [N II] 122 μm/205 μm values (see Section 3.2).

The overall change after correcting for the contribution from ionized gas is small. This is consistent with the finding of Croxall et al. (2017) that the neutral fraction of gas traced by [C II] increases with decreasing metallicity in the Beyond the Peak subsample of KINGFISH galaxies. We list the average percentages of [C II] intensity estimated to originate from the ionized gas in Table 6. The amount of emission from ionized gas can be as high as $\sim$50%, but this is only found within the H II region, where the [C II] surface brightness is low. The effect of correcting for the ionized gas mainly affects the structure of [C II] emission in and near the H II regions, where we expect little to no molecular gas.

4.2. $I_{\rm [C\,II]}$ Contribution from Atomic Gas

We estimate the amount of [C II] emission from H I by using the typical temperature and density for the conditions of the gas and assume that the column density of ionized carbon scales with the carbon abundance such that $N_{\rm C^+} = $ (C$^+$/H)$_{\rm SMC} N_{\rm H\,I}$. The [C II] emission from atomic hydrogen gas arises from a combination of the WNM, with typical temperatures of 6000–12,000 K, and the denser CNM, which has temperatures of 50–120 K. Some or all of the CNM component may be directly associated with the molecular gas as a shielding layer surrounding and mixed with the outer part of the molecular cloud in the PDR. Given the differences in conditions, we make separate estimates for the [C II] emission coming from the WNM and CNM and remove both contributions from $I_{\rm [C\,II]}$.

To estimate the possible H I associated with the [C II] emission, we want to select only the H I with velocities in the observed range of the [C II] emission. However, the spectral resolution of the PACS spectrometer is $\sim$240 km s^{-1}, which encompasses almost all of the H I emission and is a much larger

range of velocities than the $\sim$15–50 km s^{-1} widths of the ^{12}CO line observations. We use the velocity-resolved observations of [C II] from the SOFIA GREAT receiver (R. Herrera-Camus et al. 2017, in preparation) as guidance to estimate the relationship between the velocity profile of the [C II] emission and the ^{12}CO throughout all our regions.

Figure 12 shows an example [C II] spectrum from a pointing in the SWBarN region with the ALMA ACA ^{12}CO $(2 - 1)$ and H I line profiles for the same region. The [C II] line is clearly resolved and shows a profile similar to the ^{12}CO and much narrower than the H I, but the full extent of the [C II] profile is $\sim$50% wider than the full extent of the ^{12}CO line profile owing to more extended wings where there is low or no ^{12}CO emission. Requena-Torres et al. (2016) present new velocity-resolved [C II] GREAT observations of the SMC star-forming regions N66, N25/N26, and N88 that also show similarity between [C II] and ^{12}CO line profiles and find the [C II] emission to be at most 50% wider than ^{12}CO, and significantly narrower than that of H I. Similarly, comparison of the dynamics of [C II], H I, and CO on larger scales shows that the [C II] line widths agree better with the CO than H I (de Blok et al. 2016). The width of the H I line profile is due to emission from multiple kinematic components that are likely spatially separate, and the narrow profiles of the ^{12}CO and [C II] appear to originate from only one of those kinematic components. To select the H I associated with the strong [C II] emission and the molecular cloud, we created integrated intensity maps of H I for each of the ALMA regions using a velocity range that is centered on the ^{12}CO line velocity, but $\pm$25% wider than the range of velocities with observed ^{12}CO throughout the region (not for individual lines of sight) to account for the possibility of $\sim$50% wider extent of the [C II] line profile (mostly found in the wings of the line). We use these H I maps to estimate the amount of [C II] emission associated with neutral atomic gas.

To estimate the [C II] emission attributable to atomic gas, we assume a single temperature and density for each of the WNM and CNM. The H I emission will be dominated by the WNM component, which we assume to have a temperature of $\approx$8000 K (Wolfire et al. 2003) and a typical density range of 0.1–1 cm^{-3} (Velusamy et al. 2012). We set $n_{\rm WNM} = 1$ cm^{-3} for our estimate to ensure that we do not underestimate the [C II] contribution from the WNM. The C$^+$ excitation critical density for $T \approx 8000$ K of the WNM from hydrogen atoms is $n_{\rm crit}(H^0) = 1600$ cm^{-3} (Goldsmith et al. 2012). For the CNM, we assume $n_{\rm CNM} = 100$ cm^{-3} and $T = 40$ K based on the values found from the H I absorption line study by Dickey et al. (2000). For collisions with electrons, we take $n_{\rm crit,e} = 6$ cm^{-3}. We calculate the critical density for collisions with hydrogen atoms for the CNM temperature using $n_{\rm crit} = A_{ul}/R_{ul}$, where A_{ul} is the spontaneous emission rate coefficient and R_{ul} the collisional de-excitation rate coefficient. Using $A_{ul} = 2.36 \times 10^{-6}$ s^{-1} and the fit to R_{ul} for 20 K $\leqslant T^{\rm kin} \leqslant$ 2000 K from Barinovs et al. (2005), we find $n_{\rm crit}(H^0) \approx 3000$ cm^{-3}.

We calculate $I_{\rm [C II]}$ using Equation (9) for collisions with both hydrogen atoms and electrons in the WNM and CNM and collisions with H$_2$ for the CNM and add them to produce our estimate. We take an ionization fraction in neutral gas to be $n_{e^-}/n_H = 4.3 \times 10^{-4}$ (Draine 2011). In order to calculate this, we need the fraction of WNM and CNM in our lines of sight, which is unknown. We assume that 50% of $N_{\rm H I}$ associated with the CO emission is associated with the CNM and the other 50% with the WNM when calculating $I_{\rm [C II]}$. Dickey et al. (2000)

find the fraction of cool H I to be $\sim$15% of the total H I in the SMC along a few lines of sight; however, locally it may be much higher. Assuming a higher fraction of CNM will generate a higher estimate of the associated [C II] emission, decreasing the likelihood of underestimating the [C II] emission from H I. Table 6 shows the average amount of total [C II] emission for each region. We find that H I typically only accounts for $\lesssim$5%. When we apply statistical correction for optically thick H I from Stanimirović et al. (1999) to $N_{\rm H I}$ used to estimate the [C II] emission from H I, the fraction of the total [C II] emission coming from H I only slightly increases (e.g., the average increases from 2% to 3% for the SWBarN region). The SWDarkPK region has the highest fraction of [C II] emission coming from H I, likely because it is not actively forming stars and is more atomic dominated (as also suggested by the lower CO emission indicating less molecular gas at $A_V > 1$ than the other regions). These low fractions of [C II] emission from atomic gas are consistent with the theoretical study by Nordon & Sternberg (2016), who find that most of the C$^+$ column would be associated with H$_2$ gas.

4.3. Converting $I_{\rm [C II]}$ to $N_{\rm H_2}$

After removing the contributions from ionized and neutral atomic gas, we assume that the remainder of the [C II] emission originates from molecular gas. We estimate the amount of H$_2$ gas from the remaining [C II] emission in two ways:

1. Assuming a fixed T and n representative of PDR regions and converting $I_{\rm [C II]}$ to $N_{\rm H_2}$ using Equation (9).
2. Using PDR models tuned to the SMC conditions (see Appendix A) to estimate n and the FUV radiation field intensity from the observed combination of [C II], [O I], and FIR continuum, determining $N_{\rm H_2}$ from the cooling curve.

We explain both methods in the following sections.

4.3.1. Method 1: Fixed T, n

Using Equation (9), we can solve for the H$_2$ column density given the [C II] intensity:

$$N_{\rm H_2} = \frac{4.35 \times 10^{23}}{({\rm C/H})_{\rm SMC}} \left[\frac{1 + 2e^{-91.2/T} + n_{\rm crit}({\rm H_2})/n}{2e^{-91.2/T}} \right] I_{\rm [C II],H_2}.$$

(12)

To estimate $N_{\rm H_2}$, we need only assume a temperature and volume density and calculate the appropriate critical density for collisions with H$_2$ using the latest collisional de-excitation rate fits by Wiesenfeld & Goldsmith (2014) as a function of temperature, which includes H$_2$ spin effects in LTE:

$$n_{\rm crit} = \frac{A_{ul}}{R_{ul}} = \frac{2.36 \times 10^4}{4.55 + 1.6e^{(-100.0\,{\rm K}/T)}}.$$

(13)

Our assumption is that all of the [C II] emission associated with H$_2$ comes from the PDRs, where the gas is warm and moderately dense. We can then make the simplifying assumption that this region has a single average temperature of $T = 90$ K and density of $n = 4000$ cm^{-3} (consistent with the PDR modeling results in Section 4.3.2). These are chosen as similar to the excitation temperature and critical density of the transition, and thus at about the point where the gas emits

most efficiently. For reference, the exact critical density for collisions with H_2 at $T = 90$ K is $n_{\rm crit}(H_2) = 4648$ cm^{-3}. This choice of temperature and density results in a conservative estimate of the amount of molecular gas associated with the [C II] emission. Assuming a lower temperature or density would decrease the amount of [C II] emission per H_2 molecule and increase the amount of molecular gas needed to explain the observed emission, while increasing the temperature or density will not change our results significantly. The benefit of this methodology is its simplicity and straightforward calculation. The drawback is that it over simplifies the conditions of the [C II]-emitting gas by assuming only one constant temperature and volume density throughout each region and across all regions.

4.3.2. Method 2: PDR Model

We can constrain the physical conditions of the gas in the PDRs by modeling the [C II], [O I], and total FIR emission from the *Spitzer* and *Herschel* imaging. We use new PDR models generated using the elemental abundances and grain properties for SMC conditions that are presented in Appendix A. The models solve the equilibrium chemistry, thermal balance, and radiation transfer through a PDR layer characterized by a constant H nucleus volume density (n in units of cm^{-3}) and incident FUV (6 eV $< E < 13.6$ eV) radiation field (G_0 in units of the local Galactic interstellar FUV field found by Habing, 1.6×10^{-3} erg cm^{-2} s^{-1}). The models are based on Kaufman et al. (2006) but are updated for gas and grain surface chemistry as described in Wolfire et al. (2010) and Hollenbach et al. (2012). We also modify the grain properties and abundances as appropriate for the SMC (see Appendix A), which makes it tailored to modeling the emission from the HS^3 regions.

We use the [C II], [O I], and TIR intensity images as inputs to determine the nearest volume density and FUV radiation field strength in the model grids using a version of the PDR Toolbox (Pound & Wolfire 2008) that is updated with the SMC models. While the PDR Toolbox and models call for FIR intensity as the input, the term FIR is meant to represent all of the FUV and optical emission absorbed by dust and re-radiated in the infrared, which makes the current definition of TIR the most appropriate to compare to the models. We convolve the [C II] and [O I] images to the resolution of the TIR. We run the PDR Toolbox for the intensities at each matched pixel in the images and produce maps of n and G_0. The images are then sampled with $\sim$1 pixel per beam, matching the [C II] beam-sampled images. While the limiting resolution of the TIR map is lower ($\sim$18$''$) than the [C II] ($\sim$12$''$), it is not significantly lower, and we expect n and G_0 to vary smoothly. The initial images of n and G_0 show artifacts from the FIR image (due mostly to the strong beam patterns from the point sources). We take one final step and mask out regions in the images with unphysical values of n or G_0 that are due to the artifacts and use a linear interpolation to replace the masked values. The results of model fits are shown in Figure 14. The PDR models suggest that the typical volume densities are $n \sim 10^3$–10^4 cm^3, which is consistent with most of the gas being molecular in order to reproduce the observed FIR emission.

Using the maps of n and G_0, we convert the [C II] emission to N_{H_2}. We use [C II] cooling rates as a function of n that are adapted from Wolfire et al. (2003) to account for the conditions

of the SMC, which we show in Figure 15 (M. Wolfire et al. 2017, in preparation). We use the same abundances as for the PDR model. The [C II] rates are calculated for a fiducial FUV radiation field strength of $G_0 = 5.5$, which is approximately the average in diffuse gas (outside of the regions we mapped) in the SMC Southwest Bar based on the maps from Sandstrom et al. (2010), and the cooling rates were primarily intended for use in diffuse gas. While the [C II] cooling rate is only determined for a single G_0, the effect of different G_0 is to change the photoelectric heating rate, which to first order is proportional to G_0 (Bakes & Tielens 1994, Equation (42)). If [C II] dominates the cooling, then the [C II] line intensity is proportional to G_0. The appropriate [C II] cooling rate per H_2 molecule for each pixel is determined by taking the [C II] cooling rate appropriate for the specific value of n and then scaling it linearly by the ratio of estimated G_0 to the fiducial G_0 for diffuse gas. We then use this local [C II] cooling rate to calculate an H_2 column density and produce the final map. The benefit of this method is that it can account for the variations in density and radiation field in the [C II]-emitting gas throughout the regions. The weakness is that the gas conditions are estimated using "single-component" models based on plane-parallel PDRs that do not account for complex geometries, or for distributions of n or G_0 within a spatial resolution element. This is alleviated by the fact that our physical resolution is 4 pc; thus, we expect the conditions in a beam to be relatively uniform and simple "single-component" models to be more applicable than they would be if applied to data on much larger scales.

4.4. Converting I_{CO} to N_{H_2}

Once enough shielding from dissociating radiation is built up at high A_V, carbon will mostly exist in the form of CO. The exact amount of H_2 traced by the ^{12}CO emission (and not [C II]) cannot be easily calculated theoretically and relies on empirical calibrations of the conversion factor from ^{12}CO intensity to N_{H_2}, X_{CO}, typically calibrated in terms of ^{12}CO $(1 - 0)$ emission. The exact definition of X_{CO} varies depending on the study, where it can refer to the total amount of H_2 gas associated with the CO emission, including the H_2 associated with [C II] or [C I] (e.g., unresolved CO observations), or it can refer to the molecular gas only associated with gas where the dominant form of carbon is CO. For this work, we use the latter as our definition since our observations resolve the CO emission and we are separately accounting for the H_2 gas, where carbon is mostly [C II]. To convert from ^{12}CO $(2 - 1)$ to the equivalent ^{12}CO $(1 - 0)$ integrated intensity, we assume thermalized emission, which is supported by SEST observations in this region of the SMC that find ^{12}CO $(1 - 0)/^{12}$CO $(2 - 1) \sim 1$ (Rubio et al. 1993a). This is equivalent to assuming constant integrated intensity in K km s^{-1} units, or to dividing the 2–1 emission in units of W m^{-2} Hz^{-1} by $J_u^3 = 8$. Numerical simulations of low-metallicity molecular clouds show that the conversion factor reaches Galactic, high-metallicity values in the CO-bright regions (Shetty et al. 2011; Szűcs et al. 2016), suggesting that, regardless of metallicity, CO traces a similar amount of H_2 at high A_V. Given the simulation results and our estimates of X_{CO} (see Section 3.6), we use a Galactic CO-to-H_2 conversion factor $X_{CO} = 2 \times 10^{20}$ cm^{-2} (K km^{-1} s^{-1})$^{-1}$ (Bolatto et al. 2013) to estimate the amount of molecular gas present in regions at high A_V, where most of the carbon is in the form of CO. This is
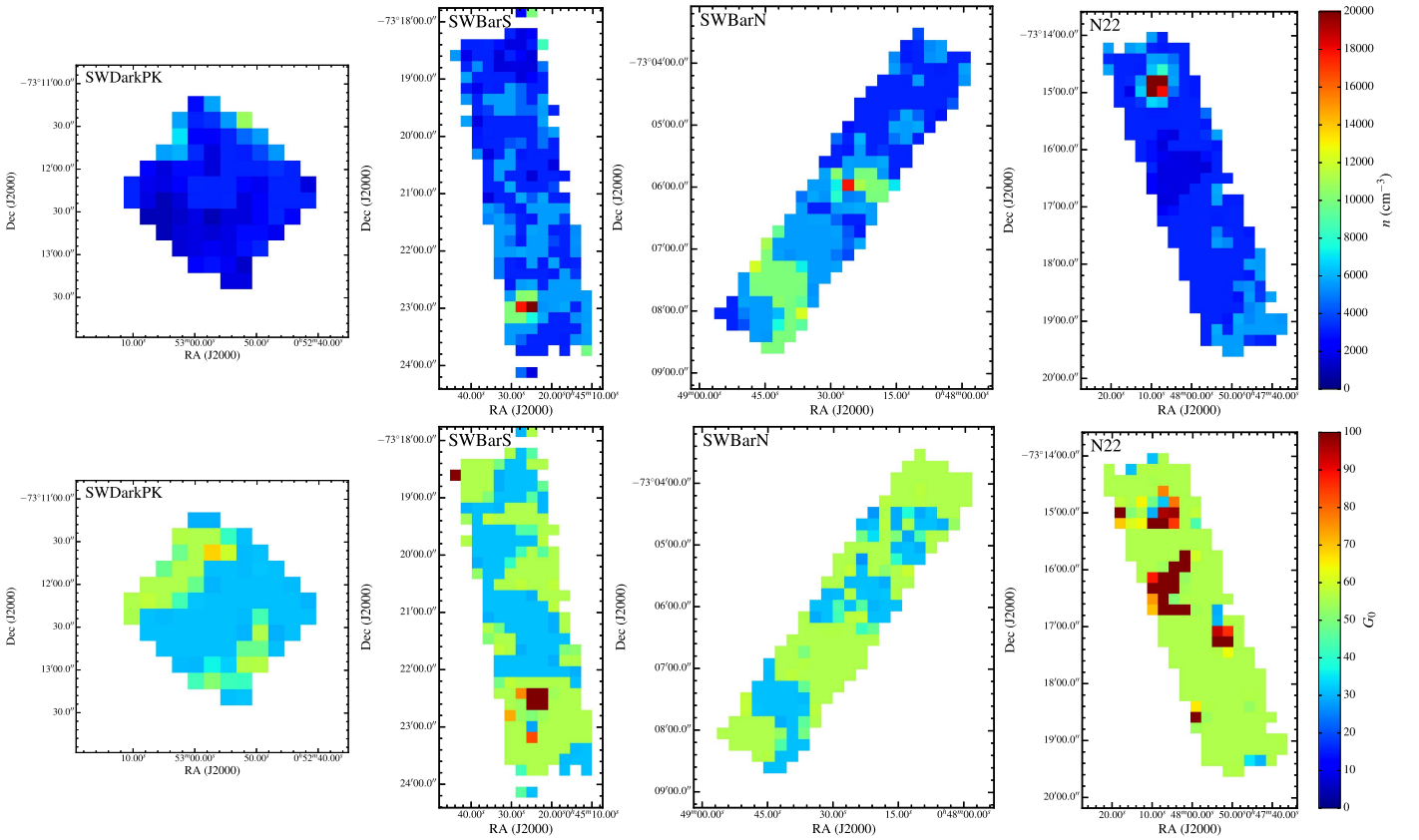
Figure 14. Density and radiation field for each of the regions with HS^3 and ALMA data, obtained from physical PDR modeling developed for the conditions in the SMC (abundances, cosmic-ray rates, dust-to-gas ratio, etc.; see Appendix A). The top row shows volume density (n). The bottom row shows FUV radiation field strength (G_0).
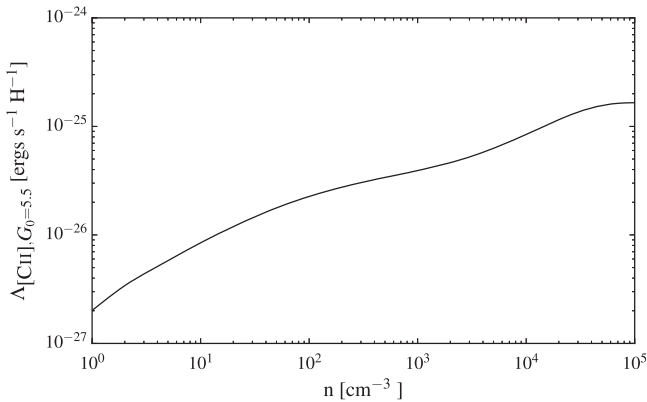

Figure 15. [C II] cooling rate ($\Lambda_{[C II]}$) as a function of density for the conditions in the SMC from M. Wolfire et al. (2017, in preparation) used to convert the [C II] emission to a column density of H_2. The cooling curve is calculated assuming $G_0 = 5.5$.

consistent with an underlying picture where most of the difference in the conversion factor observed in low-metallicity systems is due to the shrinking of the high-A_V CO-emitting cores and the growth of the outer layer of H_2 coextensive with C^+ (e.g., Wolfire et al. 2010; Bolatto et al. 2013).

4.5. N_{H_2} Estimates

Overall, the two different methods to estimate N_{H_2} based on [C II] emission produce similar results. Table 6 shows that average column densities and total H_2 masses for both methods are different by at most a factor of $\sim$1.5. The total mass

estimates from Method 1, assuming $T = 90$ K and $n = 4000$ cm^{-3}, are higher than the estimates from Method 2, using the SMC PDR models and M. Wolfire et al. (2017, in preparation) [C II] cooling rates, except for the SWDarkPK region. The fixed temperature and density produce higher estimates because they fail to account for the presence of higher-density regions that have a higher emission of [C II] per unit H_2 mass, as we show in the example in Figure 16. The opposite is true for SWDarkPK, where the densities from the PDR modeling are somewhat lower than those in other regions, and the assumed $n = 4000$ cm^{-3} in Method 1 appears to be too high. This is consistent with the observed lower level of CO emission in that very quiescent region, which is suggestive of less dense molecular gas.

The Method 1 results produce structure that is similar to the [C II] emission, with the peak in the N_{H_2} occurring at the peaks in [C II] emission, which are nearly coincident with the peaks in the CO emission. When the variations in density and radiation field strength are accounted for in the estimate in Method 2, the peaks in the N_{H_2} maps occur around the peak in the CO emission (see Figure 16), consistent with our understanding that [C II] emission should trace the H_2 gas in the PDRs surrounding the dense molecular gas traced by bright CO. We prefer the N_{H_2} estimates from Method 2 because it incorporates additional information, and we use them for the remaining analysis and discussion.

Figure 17 shows the H_2 maps derived from [C II] alone, from CO alone, and the total corresponding to their sum for each region. The H_2 estimated from [C II] is more extended than that derived from CO and wraps around it, which agrees with the
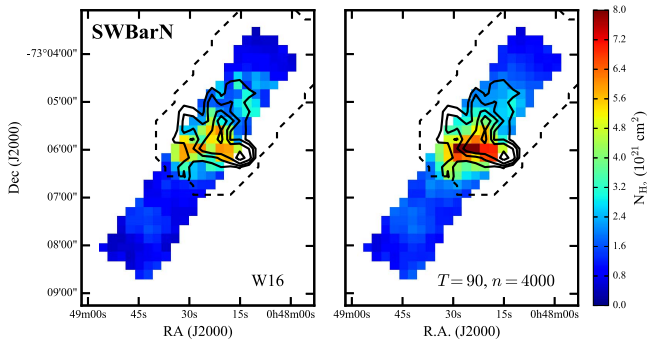
Figure 16. Images of the estimate of $N_{\mathrm{H_2}}$ from the [C II] emission for the SWBarN region using Method 2 with M. Wolfire et al. (2017, in preparation) models (left) and Method 1 with a fixed $T = 90$ K and $n = 4000$ cm^3 (right), shown at the same scale. The black contours show the estimate of $N_{\mathrm{H_2}}$ from ^{12}CO (using $X_{\mathrm{CO}} = 2 \times 10^{20}$) at levels of 0.4, 0.8, 1.4, and 2.4×10^{21} cm^{-2}, and the black dashed line shows the coverage of the ^{12}CO map. Both $N_{\mathrm{H_2}}$ estimates from [C II] produce similar average estimates of $N_{\mathrm{H_2}}$, but the structures are different. When taking into account the local T and n using the M. Wolfire et al. (2017, in preparation) results, there is less H_2 needed to explain the [C II] emission at the center of the cloud (the peak of the ^{12}CO emission). The estimated $N_{\mathrm{H_2}}$ peaks away from the ^{12}CO peak, which is consistent with the [C II] emission tracing the CO-faint H_2 in the photodissociation region, suggesting that the H_2 estimates using the new models are more accurate.

idea that the [C II] should be primarily tracing the H_2 in the low-A_V portion of the molecular cloud. The CO emission traces between ~5% and 60% of the total molecular gas in this methodology, with a typical percentage of only 20%. Note, however, that there are no H_2 column density peaks without CO emission.

4.5.1. Estimating Uncertainties

The possible sources of systematic uncertainty in our H_2 estimate using [C II] include the PACS spectrometer calibration, the uncertainty on the carbon abundance measurement, the possibility of minor [O I] absorption and [C II] optical depth, and the uncertainty in the assumptions in the low-metallicity version of the PDR model. In Table 7 we summarize the amount of uncertainty associated with each factor, and we explain how each factor is estimated in detail in Appendix B. Each of the main factors tend to contribute ⩽30% in uncertainty: ~±30% from the PACS spectrometer calibration, ~±30% from the carbon abundance measurements, and ~±20% from the combination of the effects of [O I] absorption and [C II] optical depth. Adding the results in quadrature produces a total uncertainty estimate of ~±50%. Although formally adding the uncertainties in quadrature is not necessarily correct, this gives us a reasonable estimate of the possible effect of the combined systematics. This uncertainty neglects the factor of ~2 difference in the H_2 masses measured using the higher-metallicity PDR models from Kaufman et al. (2006). The difference in the PDR models is driven by the different assumptions about dust grains compared to the Milky Way. One factor is the PAH abundance, which the SMC PDR models assume is $1/7.7$ times the Milky Way value based on the results from modeling of the mid-infrared spectra PAH band ratios using the Draine & Li (2007) models in the SMC from Sandstrom et al. (2010). However, there is a large amount of scatter in the estimated PAH abundance in the SMC, ranging from $1/2$ to $1/10$ times the Milky Way value, and the regions we mapped in the Southwest Bar show the highest PAH

abundances. A higher PAH abundance in our regions would cause the estimated H_2 masses to be higher and closer to the ones produced using the higher-metallicity PDR models. In addition to the PAH abundance, there are a number of other assumptions used for the SMC PDR models that are uncertain, and the high-metallicity PDR model results that are a factor of ~2 higher likely offer an upper limit on the H_2 mass estimates. Taking this into consideration, we choose to adopt an uncertainty of a factor of ~2 for the mass of H_2.

5. Discussion

We have presented the results of our new FIR emission line data, focusing primarily on the [C II] 158 μm and [O I] 63 μm lines from *Herschel* PACS observations, and ALMA ACA CO $(2 - 1)$ data for a sample of star-forming regions in the SMC. Using the [C II] and ^{12}CO line emission, we estimated the total amount of molecular gas in a low-metallicity environment and found that the bulk of the molecular gas is traced by [C II]. Here, we compare the [C II]-based molecular gas estimates to previous dust-based estimates, discuss the implications of [C II] molecular gas estimates and how it relates to CO, and use the [C II]-based estimates to estimate the CO-to-H_2 conversion factor (X_{CO}) and compare to simulations and models of molecular clouds at low metallicity.

5.1. Comparison to Dust-based H_2 Estimates

Another method that can trace "CO-faint" molecular gas is to use dust emission and a self-consistently determined gas-to-dust ratio in atomic regions using H I emission (Israel 1997; Dame et al. 2001; Leroy et al. 2009; Bolatto et al. 2011). We compare our molecular gas estimates using [C II] and CO with the recent dust-based molecular gas estimates for the SMC presented in Jameson et al. (2016). Table 8 shows the [C II] +CO and dust-based molecular gas estimates over the area with both [C II] and ALMA ^{12}CO coverage, where we make a cut at the rms level before calculating the total mass from CO.

The [C II]+CO estimates are not inconsistent with the dust-based estimates from Jameson et al. (2016) in the N22, SWBarN, and possibly the SWBarS regions, given the factor of ~2 uncertainty in either method. The [C II]+CO estimates for the SWDarkPK and N83 regions, on the other hand, are significantly lower than the result of the dust method. All of the [C II]+CO estimates are systematically lower than the dust-based H_2 mass estimates. The systematically lower [C II]+CO estimates can be the result of our [C II] methodology under-estimating the amount of H_2, or the dust methodology overestimating the total molecular gas mass.

When estimating the amount of H_2 associated with [C II], we have been conservative in our estimates of the contribution to [C II] from the ionized and neutral gas and the conditions of the gas (n and G_0), which may cause us to underestimate the total H_2. The dust-based method has a number of systematic uncertainties (for more details, see Leroy et al. 2007, 2009, 2011; Bolatto et al. 2011; Sandstrom et al. 2013; Jameson et al. 2016), with the two main uncertainties being the assumptions surrounding the gas-to-dust ratio and the FIR dust emissivity. In particular, the method from Jameson et al. (2016) relies on self-consistently calibrating the gas-to-dust ratio in the atomic gas, assuming that it only varies smoothly on large scales (500 pc). This methodology could overestimate the molecular gas if the gas-to-dust ratio is an overestimate of
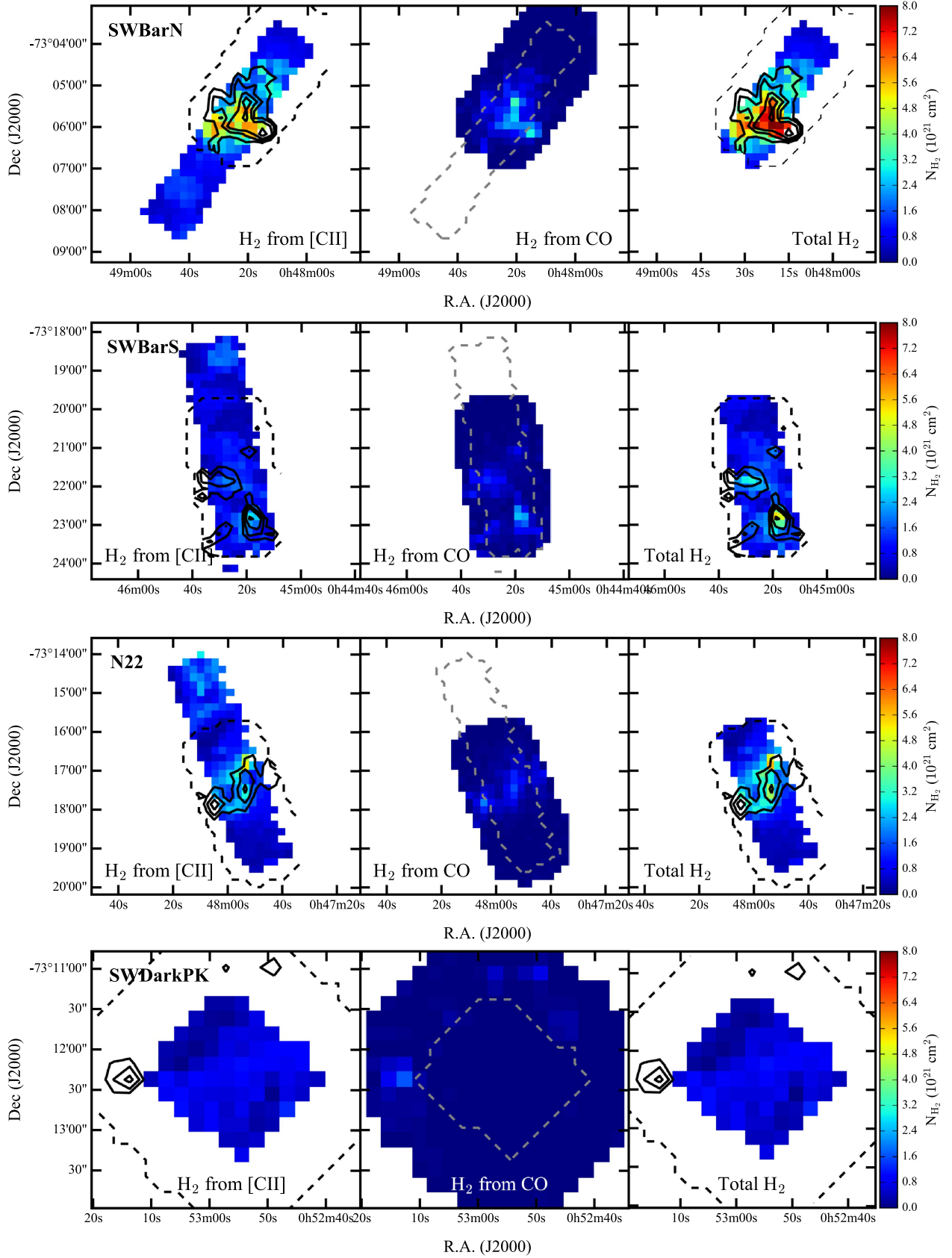
Figure 17. Images of N_{H_2} for each of the regions with *Herschel* and ALMA data. The images on the left show the estimate of N_{H_2} from the [C II] emission using Method 2 (W16 n, G_0) described in Section 4.3.2. The middle images show N_{H_2} traced by ^{12}CO, with the ALMA $(2 - 1)$ converted to $(1 - 0)$ assuming thermalized emission, and assuming a Galactic X_{CO} of 2×10^{20} cm^{-2} (K km s^{-1})$^{-1}$. The images on the right show total N_{H_2} found by combining the estimate from [C II] with the estimate from ^{12}CO. The black contours show the estimate of N_{H_2} from ^{12}CO at levels of 0.4, 0.8, 1.4, and 2.4×10^{21} cm^{-2}, and the black dashed line shows the coverage of the ^{12}CO map. The gray dashed line shows the HS^3 ([C II] and [O I]) coverage. All maps are shown at the same color scale.

Table 7
H$_2$ Estimate from [C II] Uncertainties

Source of Uncertainty	Uncertainty Estimate
PACS Calibration	±30%
Carbon Abundance	±30%
[O I] Absorption	−30%
[C II] Optical Depth	+10%
PDR Model Metallicity	Factor of 2

Table 8
Total Gas Masses

| Region | M_{H_2} ($10^5 M_\odot$) | | $M_{H I}$ ($10^5 M_\odot$) | |
	[C II]+CO	Dust	Δv_{CO}[a]	Δv_{total}
SWBarS	$0.52^{+0.52}_{-0.26}$	$2.33^{+2.33}_{-1.17}$	3.42	6.53
N22	$0.48^{+0.48}_{-0.24}$	$1.23^{+1.23}_{-0.62}$	3.15	7.30
SWBarN	$0.86^{+0.86}_{-0.43}$	$1.61^{+1.61}_{-0.81}$	4.64	9.00
SWDarkPK	$0.11^{+0.11}_{-0.06}$	$1.79^{+1.79}_{-0.90}$	1.46	3.08
N83	$0.48^{+0.48}_{-0.24}$	$2.96^{+2.96}_{-1.48}$	4.67	6.16

Note.
[a] Using the H I integrated intensity only around the velocity channels with CO emission.

the actual gas-to-dust ratio, which could be the case if the gas-to-dust ratio decreases in molecular regions. Similarly, the dust properties may vary from the diffuse to dense gas, which could produce a similar effect to a decrease in the gas-to-dust ratio.

There is also a systematic uncertainty of $\gtrsim 0.3$ dex in the dust-based molecular gas estimate. Bot et al. (2004) compared *IRAS* observations of the FIR dust emissivity in the diffuse gas with extinction studies in the SMC and found evidence for a factor of 2–3 decrease in the gas-to-dust ratio in dense gas. Roman-Duval et al. (2014) found that at the resolution of the NANTEN observation (2.6), the degeneracy between the gas-to-dust ratio, effect of dust emissivity, and X_{CO} is too large to provide definitive evidence of a change in the gas-to-dust ratio between the diffuse and molecular gas in the SMC, but allows for up to a factor of $\sim 2-3$ decrease in the gas-to-dust ratio between the diffuse and dense gas. Using depletion measurements based on FUV spectra to estimate the gas-to-dust ratio in the SMC, Tchernyshyov et al. (2015) find evidence for up to a factor of ~ 5 decrease in the gas-to-dust ratio from the diffuse to dense gas. However, these results are based on difficult measurements and rely on a number of assumptions. Jameson et al. (2016) found that scaling down the gas-to-dust ratio by a factor of 2 in the dense gas leads to a similar factor of ~ 2 decrease in the total molecular gas mass estimate. If the dust-based molecular gas estimates were lower by a factor of ~ 2, which is a possibility given the existing measurements, then all of the dust estimates would be consistent with the [C II]+CO estimates, and there would be one region (SWBarN) where the [C II]+CO molecular gas estimate would be higher than the dust-based estimate. Similarly, if we used the density and radiation field estimates from the higher-metallicity PDR models, the [C II]+CO estimates would be $\sim 2\times$ higher and would no longer be systematically below the dust-based estimates.

5.2. [C II] as a Tracer of H$_2$ and Star Formation Rate at Low Metallicity

On larger scales and in high-metallicity environments, [C II] acts as a calorimeter, as it is the main coolant of the ISM. The heating comes from FUV photons causing electrons to be ejected from dust grains owing to the photoelectric effect. Most recently De Looze et al. (2014) and Herrera-Camus et al. (2015) have shown that [C II] emission correlates well with other star formation rate (SFR) tracers, specifically Hα and 24 μm, on kiloparsec scales in nearby galaxies. On smaller scales Kapala et al. (2015) found that the correlation between [C II] and SFR holds, although much of the [C II] emission in M31 comes from outside of star-forming regions, as the FUV photons that heat the gas travel long distances diffusing throughout the gas disk. When the M31 observations are averaged over kiloparsec scales, Kapala et al. (2015) recover the relationship between [C II] and SFR observed in other galaxies.

Both De Looze et al. (2014) and Herrera-Camus et al. (2015) show that the scatter in the correlation between [C II] and SFR increases as the metallicity decreases. The breakdown in the tight [C II]–SFR relationship can be understood in terms of a decrease in the photoelectric heating efficiency and/or an increase in the FUV photon escape fraction. In a low-metallicity environment there is less dust, allowing FUV photons to propagate farther through the gas and potentially escape the region or even the galaxy. Cormier et al. (2015) find evidence of an increased UV escape fraction based on the observed O III/L_{TIR} for the DGS. The increase in the propagation distance causes the [C II] emission to be less co-localized with the recent massive star formation. If the FUV propagation distance is longer than the scale on which the [C II] emission is compared to other star formation indicators, that increases the scatter in the [C II]–SFR relationship. When the propagation distance is larger than the scale of the gas disk, a fraction of the FUV photons escape the galaxy. The [C II] emission will then underestimate the SFR even when considering integrated properties. This is consistent with the lower [C II] emission per unit SFR (estimated from combined FUV and 24 μm emission) observed at lower metallicities by De Looze et al. (2014).

On small scales, [C II] reflects the cooling of the gas and can trace the H$_2$ by accounting for the amount of emission attributed to collisions with H$_2$ molecules. This requires removing the contribution to the emission due to the cooling of the atomic gas and understanding the conditions (temperature and density) that account for the [C II] excitation. In this context, the SFR is only important in that it is the source of FUV photons that ionize the carbon and heat the PDR. Because this takes place on the scale of individual H II regions, the fraction of FUV photons that ultimately escape the galaxy does not enter in the estimates. The fact that at lower metallicity the PDR region at $A_V \lesssim 1$ is physically very extended makes [C II] an excellent tracer of "CO-faint" molecular gas. The excellent correspondence between the H$_2$ S(0) line emission and [C II] emission (see Figure 3) and the general correspondence between the [C II] and ^{12}CO emission (see Figure 11) demonstrate that [C II] traces the structure of the molecular gas at low metallicity.
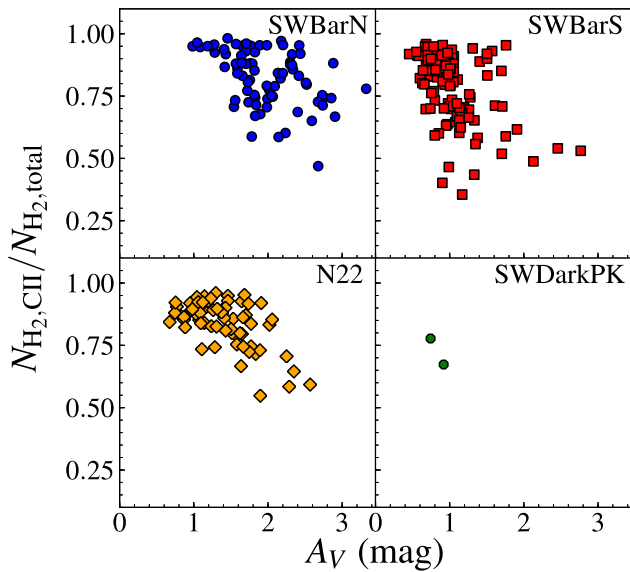
Figure 18. Relationship between $N_{H_2,[C\,II]}$ and $N_{H_2,total}$ for the ALMA regions, where $N_{H_2,total}$ is the combined estimate of H_2 from [C II] and H_2 from CO, the latter using a Galactic CO-to-H_2 conversion factor $X_{CO} = 2 \times 10^{20}$ cm^{-2} (K km s^{-1})$^{-1}$. The colored symbols show independent measurements with $I_{^{12}CO} > 3\sigma$.

Figure 19. Relationship between I_{CO} and N_{H_2} for the ALMA regions, where N_{H_2} is the combined estimate of H_2 from [C II] and from CO using the Galactic CO-to-H_2 conversion factor $X_{CO} = 2 \times 10^{20}$ cm^{-2} (K km s^{-1})$^{-1}$. The colored symbols show independent measurements detected at $>3\sigma$ in ^{12}CO. There is good correlation between CO and H_2, and the slope of the relationship is X_{CO}. The thick dashed colored lines show the linear fits to the data; the steeper slopes correspond to higher values of X_{CO}. The overplotted black dashed lines show the Galactic conversion factor (X_{CO}) appropriate for the Milky Way and resolved measurements (Bolatto et al. 2013).

5.3. Comparing [C II]-bright and CO-bright H_2

We estimated the amount of molecular gas using [C II] to trace the "CO-faint" molecular gas at low A_V ("[C II]-bright" molecular gas) and ^{12}CO to trace the molecular gas at high A_V using a Galactic X_{CO} to convert the observed emission to molecular gas ("CO-bright" molecular gas). Figure 18 shows the fraction of the total molecular gas coming from [C II] as a function of A_V estimated from dust. We see that at the low metallicity of our mapped SMC regions most of the molecular gas is traced by [C II], not CO, with ∼70% of the molecular gas coming from [C II]-bright regions on average. The data also show the expected trend of a higher fraction of the total molecular gas being traced by CO as A_V increases, although with a lot of scatter. The scatter is in part due to the fact that our A_V estimate uses data with lower resolution than the [C II] or the CO observations, and in part due to our limitations at estimating the physical conditions from the available data. But more fundamentally, much of the scatter must arise from the fact that the relevant A_V for photodissociation is not the line-of-sight extinction that we measure, but the A_V toward the dominant sources of radiation. Note that, given the methodology, the molecular gas estimate from [C II] is more likely to be underestimated rather than overestimated (see Section 4.5.1), suggesting that the "[C II]-bright" molecular fractions may be preferentially higher.

In the SWBarN and N22 regions CO traces at most ∼50% of the molecular gas at our maximum A_V. The trend in the SWBarS region is considerably steeper, and around $A_V \sim 1$ it reaches "CO-bright" fractions of ∼70%. This is consistent with the fact that this region hosts the brightest ^{12}CO and ^{13}CO emission. The range of observed "[C II]-bright" molecular gas fractions is consistent with the estimated fractions for regions in the SMC with velocity-resolved [C II] spectra by Requena-Torres et al. (2016), who find that 50% to ∼90% of the molecular gas is traced by [C II] emission. The fractions of "CO-faint" molecular gas in the SMC are much higher than

fractions found in local Galactic clouds ($f_{CO\text{-faint}} = 0.3$; Grenier et al. 2005) and fractions in dense molecular clouds estimated from [C II] emission ($f_{CO\text{-faint}} = 0.2$; Langer et al. 2014). The fractions in the SMC are more similar to those found using [C II] emission in diffuse Galactic clouds ($f_{CO\text{-faint}} = 0.75$ for clouds with no detectable ^{12}CO emission; Langer et al. 2014). Overall, the high fractions of [C II]-bright gas suggest that most of the H_2 gas in the SMC is found within PDRs or in regions with PDR-like conditions.

Figure 19 shows that, despite the fact that most molecular gas is related to [C II] rather than CO emission, our estimates for N_{H_2} are correlated with the ^{12}CO integrated intensity. The black dashed line in Figure 19 shows the estimated amount of N_{H_2} associated with CO using a Milky Way conversion factor of $X_{CO} = 2 \times 10^{20}$ cm^{-2} (K km s^{-1})$^{-1}$. There is a clear offset between the results assuming a Galactic X_{CO} and our estimate for N_{H_2}. This offset is due to the presence of molecular gas traced primarily by [C II] emission (at low A_V). Interestingly, we see that the relations are steeper than that in the Milky Way. The steeper slopes indicate that molecular gas builds up faster with CO intensity than it does in the Milky Way. This is due to the presence of "[C II]-bright" H_2 along the line of sight toward CO emission—simply the result of the fact that "CO-bright" regions still have substantial [C II] emission associated with them at the resolution of our measurements.

5.4. The CO-to-H_2 Conversion Factor in the SMC

We use our N_{H_2} determination to estimate the values of X_{CO} throughout the mapped regions, accounting for both "[C II]-bright" and "CO-bright" molecular gas. Figure 20 shows our estimates of X_{CO} as a function of A_V, where there is a trend of decreasing X_{CO} with increasing A_V albeit with significant
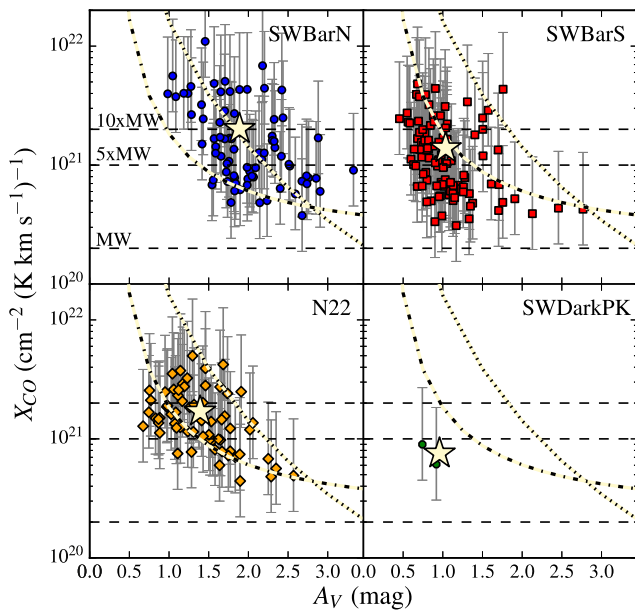
Figure 20. CO-to-H_2 conversion factor (X_{CO}) as a function of A_V for the ALMA regions, where the H_2 used is the combined estimate of H_2 from [C II] and H_2 from CO using a Galactic value of $X_{CO} = 2 \times 10^{20}$ cm^{-2} (K km s^{-1})$^{-1}$. The colored symbols show independent measurements detected at $>3\sigma$ in ^{12}CO, with the error bars showing the factor of 2 uncertainty in N_{H_2} and the star symbols showing the mean A_V and X_{CO} for each region. The overplotted dashed lines show scalings of the Galactic conversion factor appropriate for the Milky Way and resolved measurements (Bolatto et al. 2013). The dotted line shows the estimate of X_{CO}-based average CO luminosity, the average N_{H_2}, and the average A_V over the entire cloud for the simulations of molecular clouds by Glover & Mac Low (2011). The dot-dashed line shows a similar cloud-averaged estimate of X_{CO} as a function of A_V from the PDR models from Wolfire et al. (2010) for the SMC metallicity and radiation field strength of 40 G_0, the approximate mean radiation field found in the regions (see Section 4.3.2).

scatter. The trend in X_{CO} matches the expectation of extended envelopes of "[C II]-bright" molecular gas, and it compares well with similar trends seen in low-metallicity molecular cloud simulations (Shetty et al. 2011; Szűcs et al. 2016). The scatter can be explained as being due to the "breakdown" of a single value of X_{CO} on small scales in simulations and even observed clouds, due to the clumpy nature of molecular clouds (Glover & Mac Low 2011; Shetty et al. 2011; Bolatto et al. 2013).

The values we find for our regions have on average a conversion factor of $X_{CO} \sim 5 X_{CO,MW}$. For the entire SMC, and using the dust-based molecular gas estimates, Jameson et al. (2016) find a CO-to-H_2 conversion factor ~ 17 times higher than the average Milky Way value. The difference between these two results can be mostly ascribed to the bias in our chosen HS^3 fields. Our survey selected actively star-forming regions with bright CO emission, whereas most of the SMC is faint in CO; in fact, our regions contain some of the peaks of CO emission in the SMC. But even within our observed regions many lines of sight have high fractions of H_2 not traced by "bright CO" emission (see Figure 18). The higher global measurement is simply a statement of the fact that the extinction in a typical molecular line of sight in the SMC is probably $A_V \sim 0.5$–1. Accounting for the dust-to-gas ratio of $1/5$–$1/7$ the Galactic value, the same line of sight would have $A_V \sim 2.5$–7 in the Milky Way and emit brightly in CO. Even in our highly biased regions bright in CO we barely reach $A_V \sim 2.5$ in the SMC (Figure 20). Schruba et al. (2017) also found variations in the CO-to-H_2 conversion factor using

dust-based H_2 estimates in different regions of the low-metallicity dwarf galaxy NGC 6822, with the lowest values (closest to the Milky Way value) in the regions with bright CO emission. Using galaxy-integrated measurements of [C II] and ^{12}CO and isolating the [C II] contributions from molecular gas using the results of models of [C II] emission throughout a galaxy, Accurso et al. (2017) estimated the conversion factor and found the values to be in the range of ~ 12.5–$17\times$ the Milky Way value for the metallicity of the SMC, which is within the range of our estimates of X_{CO}.

We can compare our estimates of X_{CO} versus A_V with theoretical studies of the relation between CO and H_2 at low metallicity. Wolfire et al. (2010) present a model of molecular clouds in order to understand the fraction of H_2 not traced by bright CO emission as a function of metallicity. They assume spherical clouds with r^{-1} density profile, predicting the fraction of "CO-faint" gas based on their mean volume density, external radiation field, mean A_V ($\langle A_V \rangle$), and metallicity relative to Galactic (Z'). Glover & Mac Low (2011) and more recently Szűcs et al. (2016) created simulations of molecular clouds with varying conditions, including metallicity, finding an empirical relationship for the mean X_{CO} value as a function of the mean A_V for the simulated clouds. The trend predicted by the Wolfire et al. (2010) calculations and formulated by Bolatto et al. (2013) is

$$X_{CO} = X_{CO,0} e^{(4\Delta A_V / \langle A_V \rangle)} e^{(-4\Delta A_V / (\langle A_V \rangle / Z'))}, \quad (14)$$

where

$$\Delta A_V = 0.53 - 0.045 \log\left(\frac{G_0}{n}\right) - 0.097 \log(Z'), \quad (15)$$

while Glover & Mac Low (2011) find

$$X_{CO} = \begin{cases} X_{CO,0}(\langle A_V \rangle / 3.5)^{-3.5} & \text{if } \langle A_V \rangle < 3.5 \text{ mag} \\ X_{CO,0} & \text{if } \langle A_V \rangle \geq 3.5 \text{ mag} \end{cases}, \quad (16)$$

where $X_{CO,0}$ is the mean value for the Milky Way.

In Figure 20 we overplot the predicted X_{CO} trend from Wolfire et al. (2010) using the metallicity of the SMC ($Z' = 0.2$), an average $n = 5000$ cm^{-3}, and $G_0 = 40$ based on the PDR modeling we did (see Section 4.3.2). We also overplot the empirical fit from the simulations by Glover & Mac Low (2011). Both predictions are close to the data for both individual lines of sight and the averages within a region (indicated by the star), although Wolfire et al. (2010) seem to do a better job overall. As both the Wolfire et al. (2010) model and Glover & Mac Low (2011) simulations suggest, the main effect driving the relationship between X_{CO} and A_V is not metallicity itself, but how metallicity and environment affect the FUV shielding in the molecular gas. In particular, the critical element is the dust-to-gas ratio in the medium. This is also consistent with the findings of Leroy et al. (2009) and Lee et al. (2015) showing that the amount of ^{12}CO emission at a given value of A_V in the SMC resembles that in the Milky Way.

5.5. ^{12}CO and the Molecular-to-atomic Transition

Our new measurements present an opportunity to look at the molecular-to-atomic transition at low metallicity. We estimate the molecular-to-atomic ratio using our total molecular gas estimate, N_{H_2}, and the H I column density map associated with the molecular cloud. The $N_{H I}$ map is the same that we used to determine the amount of [C II] emission associated with H I gas
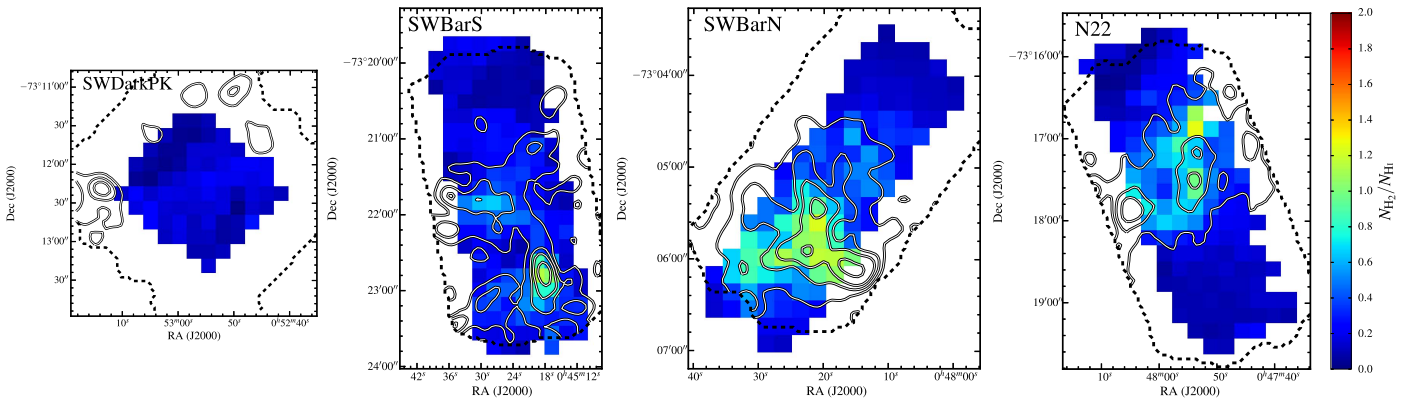
Figure 21. Ratio of the estimate of the total molecular gas column (using [C II] and ^{12}CO) to $N_{H I}$ estimated to be associated with the molecular cloud (see Section 4.2). The black contours show the ALMA ^{12}CO $(2 - 1)$ integrated intensity (convolved to [C II] resolution of 12″) at levels of 1.6 ($\sim 3\sigma$), 8, 16, 32, and 48 K km s^{-1}. We see that faint CO emission extends to $N_{H_2}/N_{H I} \sim 0.5$, which is beyond the estimated molecular-to-atomic transition.

(see Section 4.2), which was produced by only integrating the H I emission over a velocity range that is centered on the ^{12}CO line velocity, but $\pm 25\%$ wider than the range of velocities with observed ^{12}CO emission throughout each region. Figure 21 shows the maps of the $N_{H_2}/N_{H I}$ ratio with overlaid ALMA ^{12}CO contours. As expected for the atomic-dominated SMC, we observe peak molecular-to-atomic ratios of $N_{H_2}/N_{H I} \sim 1.5$ that show that the amount of molecular gas does not greatly exceed the amount of H I gas along the line of sight owing to the large amount of atomic gas. We also detect ^{12}CO emission out to $N_{H_2}/N_{H I} \sim 0.5$, which is beyond the region of the cloud where we estimate the molecular gas to dominate over the atomic gas based on the measured column densities. The observation of ^{12}CO emission out to the region where we estimate that the molecular-to-atomic transition occurs indicates that the molecular gas is truly "CO-faint" and not "CO-dark." We note, however, that trying to use CO to estimate molecular masses at low metallicities rapidly runs into the problem of the fast growth in the conversion factor and its steep dependence on local conditions, nominally A_V or column density.

6. Summary and Conclusions

We present results from HS^3, a survey that mapped FIR cooling lines in five star-forming regions. These data are complemented by APEX CO observations in the SMC Wing region N83; by ALMA ACA observations of the Southwest Bar of the SMC that mapped four of the five HS^3 regions in ^{12}CO, ^{13}CO, and C^{18}O; and by SOFIA GREAT observations that will be presented fully in a forthcoming paper. The main results from these new observations are as follows:

1. The [C II] 158 μm line is detected throughout the entirety of the regions. The [O I] 63 μm emission is also very widespread and detected throughout large portions of the regions, including faint diffuse areas (Section 3.1, Figure 1).
2. The [O I]/[C II] ratio is fairly uniform throughout all the regions, with an average value of [O I]/[C II] ~ 0.3 (Section 3.1, Figure 2).
3. We do not detect the [N II] 122 μm line, but we do detect the [N II] 205 μm line in every region with FTS spectroscopy. Using the upper limit on the [N II] 122 μm observations, the observed [N II] 122 μm/

205 μm ratio is consistent with an electron density $n_e \lesssim 20$ cm^{-3} (Section 3.2, Figure 6).
4. We find [O III]/[C II] ratios in the H II regions that are high compared to more massive, higher-metallicity galaxies (Section 3.3, Figure 7).
5. Our ALMA ACA ^{12}CO maps include the total power correction and show small (few pc), bright structures with bright ^{13}CO surrounded by more diffuse, faint emission. We do not detect C^{18}O in any of the regions. We find ^{12}CO/^{13}CO ~ 7–13, which translates to ^{12}CO optical depths of $\tau_{^{12}CO} \sim 4.5$–11 assuming that the ^{13}CO emission is optically thin (Section 3.4, Figures 8 and 9).
6. The ^{12}CO/[C II] ratios are $\sim 1/5$ the average ratio found for the Milky Way and increase with A_V, reaching the Milky Way ratio or higher. The low ^{12}CO/[C II] ratios at low A_V suggest that there is a layer of molecular gas not traced by bright ^{12}CO emission, which is confirmed by our modeling (Section 3.7, Figures 11 and 13).

We see evidence that the [C II] emission traces molecular gas in regions where the CO is expected to be photodissociated from the low ^{12}CO/[C II] ratios and good correspondence between the [C II] structure and the H$_2$ S(0) and ^{12}CO emission. We use the [C II] and ^{12}CO emission to estimate the total molecular gas assuming that the bright [C II] emission traces molecular gas at low A_V and ^{12}CO traces gas at high A_V. We first remove the possible [C II] emission from the ionized and atomic gas (both CNM and WNM) and assume that the remaining [C II] emission arises from molecular gas. We convert this emission to N_{H_2} using two different methods: the first assumes a fixed temperature and density of $T = 90$ K and $n = 4000$ cm^{-3}, and the second uses the n and G_0 from new SMC PDR models (see Appendix A) for the [C II], [O I], and TIR combined with new [C II] cooling rates from M. Wolfire et al. (2017, in preparation). The two methods produce similar results, but we choose to use the second method to account for variations in the conditions throughout the regions. We convert the ^{12}CO emission to a molecular gas estimate applicable in the high-A_V regions of the clouds using a Milky Way conversion factor of $X_{CO} = 2 \times 10^{20}$ cm^{-2} (K km s^{-1})$^{-1}$. We estimate a factor of 2 uncertainty in our molecular gas estimates, but note that, given our assumptions for the carbon abundance and PDR models, we are more likely to underestimate N_{H_2} traced by [C II].

Using our estimates of N_{H_2} using [C II] and ^{12}CO, we find the following:

1. Our H_2 column density estimated from [C II] and ^{12}CO is mostly consistent with (although systematically lower than) larger-scale dust-based estimates from Jameson et al. (2016).
2. We find average fractions of the molecular gas traced by [C II] of ~70% and show that most of the molecular gas in the SMC is not traced by bright ^{12}CO emission, which is expected for low-metallicity environments, where H_2 is able to self-shield while CO is photodissociated.
3. We use the N_{H_2} estimated from [C II] and ^{12}CO to evaluate the CO-to-H_2 conversion factor (X_{CO}) and find that X_{CO} decreases with increasing A_V. The relationship between X_{CO} and A_V is consistent with models from Wolfire et al. (2010) and simulations from Glover & Mac Low (2011) and Szűcs et al. (2016), which suggests that the main effect of lowering the metallicity is to decrease A_V and the amount of shielding for a given gas column density.
4. Despite the fact that most of the molecular gas in the SMC is not traced by bright CO emission, we do observe faint ^{12}CO emission out to the estimated location of the molecular-to-atomic transition. Using the aggregate CO emission to obtain total molecular mass in a low-metallicity environment suffers from the problem that it is very sensitive to the local A_V or column density.

Appendix A
SMC PDR Models

The PDR model we use is based on that of Kaufman et al. (2006), Wolfire et al. (2010), and Hollenbach et al. (2012), but with a modified grain extinction, grain abundances, and gas-phase abundances as appropriate for the SMC. For the gas-phase metal abundances we use 1/5 of the Galactic values. We use the conversion between optical depth and column density for the average "Bar Sample" from Gordon et al. (2003), $N/A_V = 1.32 \times 10^{22}$ cm^{-2}. For the small grain abundance, which scales the photoelectric heating rate, we use an abundance 1/7.7 of the Galactic value from Sandstrom et al. (2010). The FUV rise of the dust extinction is known to be steeper than the Galactic case (Gordon et al. 2003), which decreases the penetration of FUV photons into the PDR. The general form of the photochemical rates is $G_0 \alpha e^{(-\beta A_V)}$, where α scales the overall rate and β accounts for the dust attenuation relative to visible wavelengths. We assume that the beta coefficients for the SMC are a factor of 2 higher than for local Galactic grains. This assumption was checked using the Meudon PDR code (Le Petit et al. 2006). First, we added an SMC extinction curve to the code using the fits in Gordon et al. (2003) to the Fitzpatrick & Massa (1990) parameterized extinction curves. Second, we fit the resulting beta dependence as a function of A_V to several key rates calculated by the Meudon PDR code. We find that the factor of 2 results in less than 10% difference in α compared to the Meudon code for the rates that we tested.

Resulting contour plots for [O I] 63 μm/[C II] 158 μm and ([O I] 63 μm + [C II] 158 μm)/FIR as a function of G_0 and n are shown in Figure 22. For reference, Figure 23 shows the PDR model results using the models for Galactic conditions from Kaufman et al. (2006). Compared to the Galactic case (Kaufman et al. 1999, 2006) at fixed G_0, the contours of ([OI] 63 + [CII] 158)/FIR are generally shifted to higher density or lower G_0/n ratio. This line-to-continuum ratio can be interpreted as the heating efficiency or the fraction of energy that goes into gas heating compared to the total FUV photon energy (note that the total FIR is approximately twice the FUV energy owing to dust heating by optical photons). Theoretical models predict that in low-metallicity environments the reduced abundance of electrons from metals leads to a higher grain charge and lower heating efficiencies (e.g., Röllig et al. 2006). Increasing n, or lowering G_0/n, leads to more neutral grains and higher heating efficiencies. For low G_0 (approximately less than 10) and low densities n (approximately less than 10^3) the [O I] 63 μm/[C II] 158 μm ratio for the SMC deviates from the Galactic curves owing to the strong temperature dependence in this region and the effects of metallicity on the heating efficiency. Lower heating efficiency leads to a lower temperature, low [O I] 63 μm line intensity, and low [O I] 63 μm/[C II] 158 μm ratio (we note that at very low G_0 and high density the [C II] line intensity rapidly drops, leading to a high ratio of [O I] 63 μm/[C II] 158 μm). At higher density and G_0 the curves are similar to the Galactic case.
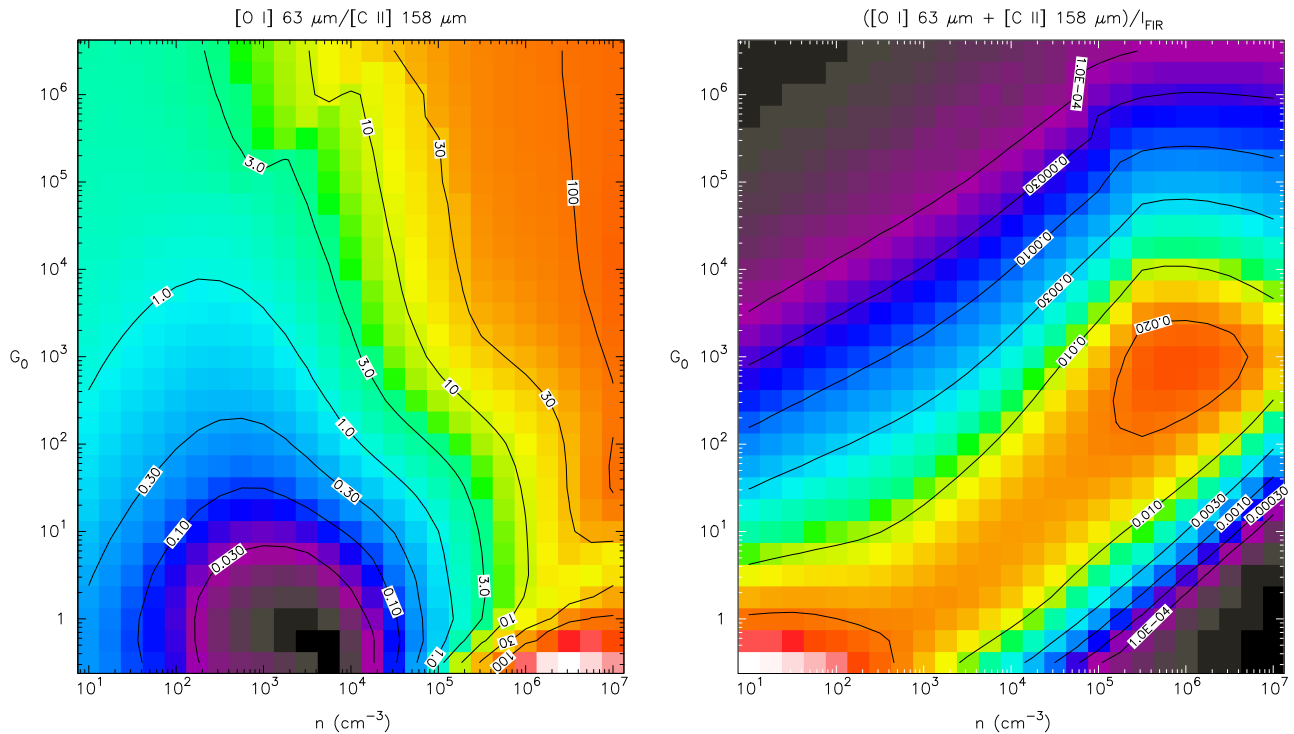
Figure 22. New SMC PDR model contour plots for the [O I] 63 μm/[C II] 158 μm (left) and ([O I] 63 μm + [C II] 158 μm)/FIR ratios as a function of n and G_0. The data used to create this figure are available.

Appendix B
H$_2$ Estimate from [C II] Uncertainties

In this section we explore the effects of different potential sources of uncertainty that could affect the H$_2$ column density estimates. We explore in detail how [O I] absorption and [C II] optical depth could affect our adopted values of G_0 and n from the models, as well as the difference between the results using the SMC PDR models and the higher-metallicity models. In general, increasing n and/or G_0 will increase the [C II] cooling rate, which decreases the amount of H$_2$ needed to account for the observed [C II] emission. The amount of increase in [C II] cooling depends on the specific value of n since it is not a linear function of n (see Figure 15), whereas the [C II] cooling scales linearly with G_0.

The values of G_0 appear to be robust to the choice of PDR model since the results using the SMC PDR models are similar to those found using the high-metallicity models from Kaufman et al. (2006) (see Appendix A). The G_0 values are also consistent with the values found by Israel & Maloney (2011) for the N22 and SWBarN (N27) regions using Lyman continuum and dust emission and by Sandstrom et al. (2010) from modeling the mid-IR SED. The results for n using the new SMC PDR models are a factor of $\sim$10 higher than what would have been obtained using a high-metallicity PDR model (e.g., Kaufman et al. 1999). For a given G_0 and n the grains will be more charged at low metallicity owing to fewer free electrons (primarily from the lower carbon abundance). The increase in grain charge will decrease the photoelectric heating efficiency, and a higher density is required to produce the observed line intensity ratios. See Appendix A for a full description of the changes in the new PDR models. This increase in density translates to an increase in the total H$_2$ mass from [C II] ($M_{H_2,[C II]}$) by factors of $\sim$1.5–3.0.

There are uncertainties associated with the interpretation of the available observations, in particular, the possibility of [O I] self-absorption and optically thick [C II] emission. We already discussed the likelihood of [O I] absorption or self-absorption in Section 3.1.1 and found no evidence that there is significant absorption present in our observations. To explore how a low level of absorption would affect our results, we assume that 30% of the integrated [O I] intensity is absorbed, leading to a 30% underestimate in the real [O I] flux. We find that if we allow for 30% larger [O I] flux, the model density increases by a factor of $\sim$3, while the radiation field G_0 decreases by a similar factor of $\sim$3. The increase in density increases the cooling rate, which decreases the amount of H$_2$ needed to explain the [C II] emission. Conversely, decreasing G_0 also decreases the cooling rate, which increases the amount of H$_2$. At the moderate densities in the regions ($\sim$10^3–10^4 cm^{-3}), the cooling rate does not increase much with n, whereas the cooling rate will scale linearly with G_0. As a result, the effect of increasing the amount of H$_2$ from the change in G_0 dominates over the decrease due to the change in n and the estimated $M_{H_2,[C II]}$ decreases by $\sim$30%.

We have no evidence that the [C II] 158 μm emission is optically thick in our SMC regions. Measurements of [^{13}C II] and [^{12}C II] in dense, Galactic PDRs find optical depths $\tau_{[C II]} \approx 0 - 3$ (Ossenkopf et al. 2013). A moderate optical depth of $\tau_{[C II]} = 1$ seen in Galactic regions scaled to account for the lower carbon abundance in the SMC gives $\tau_{[C II]} = 0.2$. This level of optical depth is also possible in the higher-N_{H_2} regions; using the equation for $\tau_{[C II]}$ from Crawford et al. (1985) with $N_{H_2} = 10^{22}$ cm^{-2} (values found in the peaks of our N_{H_2} estimates), $T = 100$ K, and $n = 5000$ cm^{-3} produces $\tau_{[C II]} = 0.2$. To explore how this level of moderate optical depth would affect our H$_2$ estimates, we correct the [C II]
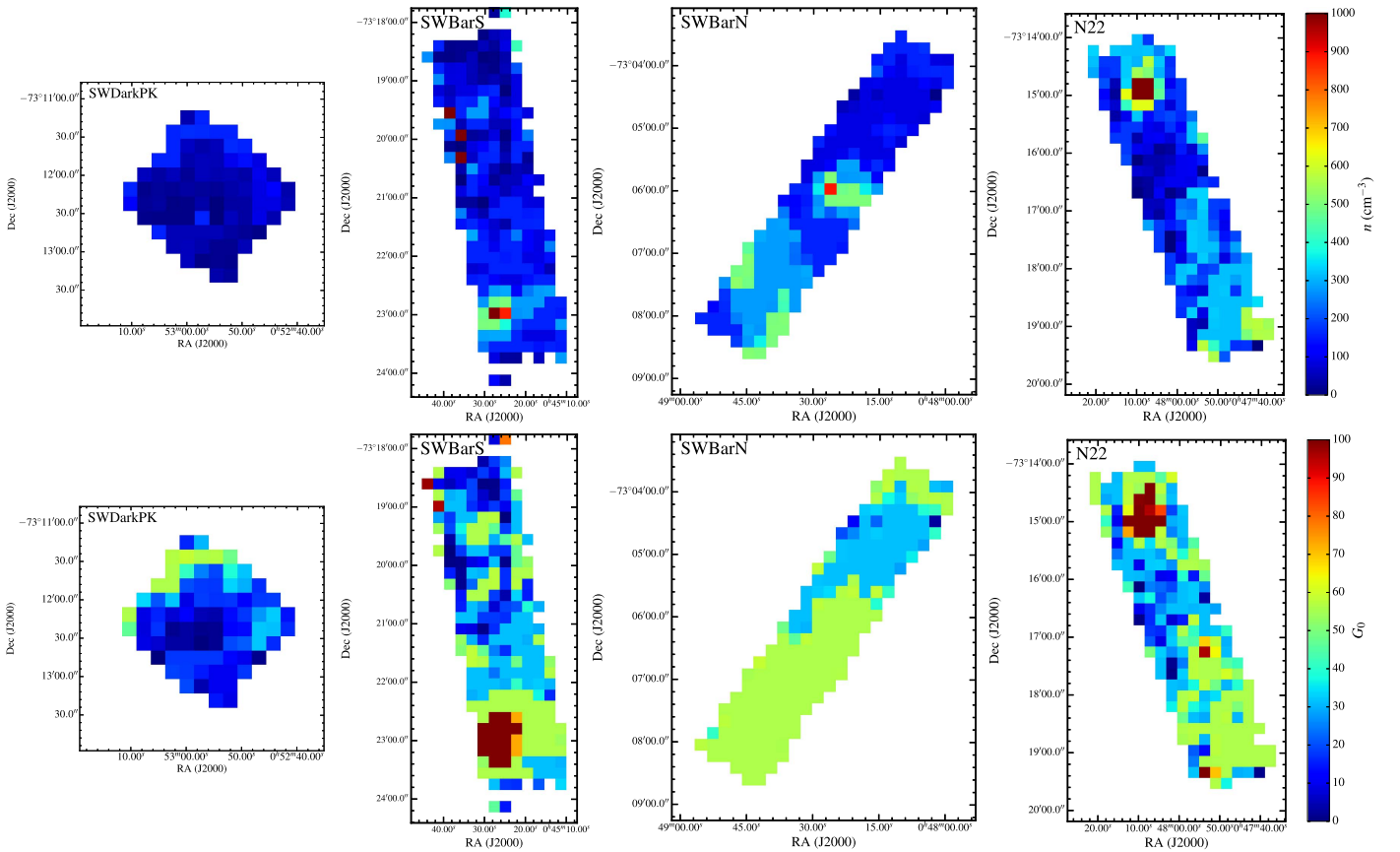
Figure 23. Images of the results using the previous PDR models for Galactic conditions from Kaufman et al. (2006) for volume density (n; top row) and FUV radiation field strength (G_0; bottom row) for each of the regions using the same [C II], [O I], and TIR data as Figure 14. These models indicate similar radiation field strengths, but the densities are a factor of $\sim$10 lower than those found using the SMC PDR models.

emission by a factor of $\tau/(1 - \exp(-\tau)) = 1.1$. We find that this has little effect on the model values of n and G_0, and only increasing n by a factor of $\lesssim 2$ in some of the denser ($n \sim 5000$–$10{,}000\,\mathrm{cm}^{-3}$) regions and decreasing G_0 by the same factor. Since n and G_0 remain largely the same, the [C II] cooling rate is the same as for the uncorrected, lower [C II] intensity, while the optical depth correction increases the amount of [C II] emission, which increases the amount of H_2. The correction for $\tau_{[\mathrm{C\,II}]} = 0.2$ increases the mass estimates by $\sim$10%.

Additional sources of uncertainty include the carbon abundance, the absolute flux calibration of the PACS spectrometer, and the [C II] intensity attributed to ionized and neutral gas. The measurements of the gas-phase carbon abundance in the SMC are in the range of C/H $\sim 1.4 \times 10^{-5} - 4.2 \times 10^{-5}$ (Kurt et al. 1999; Tchernyshyov et al. 2015). This introduces a factor of $\sim$30% uncertainty to our assumed value of 2.8×10^{-5}, which translates into a factor of $\sim$30% uncertainty in the H_2 estimate, as it scales linearly with carbon abundance. The absolute flux calibration of the PACS spectrometer is an additional source of uncertainty on the order of 30% (Poglitsch et al. 2010). Finally, there is uncertainty involved in our estimates of the [C II] intensity attributed to neutral and ionized gas. Our estimate of [C II] emission from ionized gas would likely only overestimate the actual contribution, and the ultimate contribution is small ($\lesssim$10%) in the regions in and around the molecular cloud and does not significantly affect the total H_2 mass estimate. The

contribution from neutral gas is more uncertain. Changing the amount of H I associated with the WNM has little effect on the estimated [C II] intensity owing to the high temperature and low density (compared to the critical density) of the gas, but the high temperature causes the H I emission from the WNM to dominate over the CNM. Changing the amount of H I in the CNM has a stronger effect on the attributed [C II] intensity owing to the density being closer to the critical density (see Equation (9)). Varying the fraction of the H I associated with the CNM from our assumed value of 50% to 25% and 75% changes the fraction of the [C II] intensity from neutral gas by $\pm$2%, which would ultimately have a similar effect on the mass to the optical depth correction. Since a correction to $I_{[\mathrm{C\,II}]}$ of +10% had an effect of $\sim$+10% on the mass, a $\sim$2% correction to $I_{[\mathrm{C\,II}]}$ will cause a $\sim$2% increase of the H_2 mass, which is negligible compared to the other sources of uncertainty discussed.

ORCID iDs

Katherine E. Jameson ◉ https://orcid.org/0000-0001-7105-0994
Alberto D. Bolatto ◉ https://orcid.org/0000-0002-5480-5686
Mark Wolfire ◉ https://orcid.org/0000-0003-0030-9510
Rodrigo Herrera-Camus ◉ https://orcid.org/0000-0002-2775-0595
Kevin Croxall ◉ https://orcid.org/0000-0002-5258-7224
John-David Smith ◉ https://orcid.org/0000-0003-1545-5078
Remy Indebetouw ◉ https://orcid.org/0000-0002-4663-6827

Frank P. Israel ⬤ https://orcid.org/0000-0002-6760-9449
Julia Roman-Duval ⬤ https://orcid.org/0000-0001-6326-7069
Jacco Th. van Loon ⬤ https://orcid.org/0000-0002-1272-3017

References

Accurso, G., Saintonge, A., Catinella, B., et al. 2017, MNRAS, 470, 4750
Aniano, G., Draine, B. T., Gordon, K. D., & Sandstrom, K. 2011, PASP, 123, 1218
Astropy Collaboration, Robitaille, T. P., Tollerud, E. J., et al. 2013, A&A, 558, A33
Bakes, E. L. O., & Tielens, A. G. G. M. 1994, ApJ, 427, 822
Barinovs, Ğ., van Hemert, M. C., Krems, R., & Dalgarno, A. 2005, ApJ, 620, 537
Bolatto, A. D., Jackson, J. M., & Ingalls, J. G. 1999, ApJ, 513, 275
Bolatto, A. D., Leroy, A. K., Jameson, K., et al. 2011, ApJ, 741, 12
Bolatto, A. D., Leroy, A. K., Rosolowsky, E., Walter, F., & Blitz, L. 2008, ApJ, 686, 948
Bolatto, A. D., Simon, J. D., Stanimirović, S., et al. 2007, ApJ, 655, 212
Bolatto, A. D., Wolfire, M., & Leroy, A. K. 2013, ARA&A, 51, 207
Bot, C., Boulanger, F., Lagache, G., Cambrésy, L., & Egret, D. 2004, A&A, 423, 567
Bourke, T. L., Garay, G., Lehtinen, K. K., et al. 1997, ApJ, 476, 781
Brand, J., & Wouterloot, J. G. A. 1995, A&A, 303, 851
Brauher, J. R., Dale, D. A., & Helou, G. 2008, ApJS, 178, 280
Chevance, M., Madden, S. C., Lebouteiller, V., et al. 2016, A&A, 590, A36
Cohen, R. S., Dame, T. M., Garay, G., et al. 1988, ApJL, 331, L95
Cormier, D., Madden, S. C., Lebouteiller, V., et al. 2015, A&A, 578, A53
Crawford, M. K., Genzel, R., Townes, C. H., & Watson, D. M. 1985, ApJ, 291, 755
Croxall, K. V., Smith, J. D., Pellegrini, E., et al. 2017, ApJ, 845, 96
Croxall, K. V., Smith, J. D., Wolfire, M. G., et al. 2012, ApJ, 747, 81
Dalgarno, A., & Black, J. H. 1976, RPPh, 39, 573
Dame, T. M., Hartmann, D., & Thaddeus, P. 2001, ApJ, 547, 792
Davies, R. D., Elliott, K. H., & Meaburn, J. 1976, MmRAS, 81, 89
de Blok, W. J. G., Walter, F., Smith, J.-D. T., et al. 2016, AJ, 152, 51
De Looze, I., Cormier, D., Lebouteiller, V., et al. 2014, A&A, 568, A62
Dickey, J. M., Mebold, U., Stanimirovic, S., & Staveley-Smith, L. 2000, ApJ, 536, 756
Dickman, R. L. 1978, ApJS, 37, 407
Draine, B. T. 2011, in Physics of the Interstellar and Intergalactic Medium, ed. B. T. Draine (Princeton, NJ: Princeton Univ. Press)
Draine, B. T., & Li, A. 2007, ApJ, 657, 810
Dufour, R. J. 1984, in IAU Symp. 108, Structure and Evolution of the Magellanic Clouds, ed. S. van den Bergh & K. S. S. de Boer (Dordrecht: Reidel), 353
Fitzpatrick, E. L., & Massa, D. 1990, ApJS, 72, 163
Galametz, M., Kennicutt, R. C., Calzetti, D., et al. 2013, MNRAS, 431, 1956
Garden, R. P., Hayashi, M., Hasegawa, T., Gatley, I., & Kaifu, N. 1991, ApJ, 374, 540
Glover, S. C. O., Clark, P. C., Micic, M., & Molina, F. 2015, MNRAS, 448, 1607
Glover, S. C. O., & Mac Low, M.-M. 2011, MNRAS, 412, 337
Goldsmith, P. F., Langer, W. D., Pineda, J. L., & Velusamy, T. 2012, ApJS, 203, 13
Gordon, K. D., Clayton, G. C., Misselt, K. A., Landolt, A. U., & Wolff, M. J. 2003, ApJ, 594, 279
Gordon, K. D., Meixner, M., Meade, M. R., et al. 2011, AJ, 142, 102
Grenier, I. A., Casandjian, J.-M., & Terrier, R. 2005, Sci, 307, 1292
Griffin, M. J., Abergel, A., Abreu, A., et al. 2010, A&A, 518, L3
Helsel, D. R. 2005, Nondetects and Data Analysis: Statistics for Censored Environmental Data (New York: Wiley)
Henize, K. G. 1956, ApJS, 2, 315
Herrera-Camus, R., Bolatto, A., Smith, J. D., et al. 2016, ApJ, 826, 175
Herrera-Camus, R., Bolatto, A. D., Wolfire, M. G., et al. 2015, ApJ, 800, 1
Heyer, M., Krawczyk, C., Duval, J., & Jackson, J. M. 2009, ApJ, 699, 1092
Heyminck, S., Graf, U. U., Güsten, R., et al. 2012, A&A, 542, L1
Hollenbach, D., Kaufman, M. J., Neufeld, D., Wolfire, M., & Goicoechea, J. R. 2012, ApJ, 754, 105
Hollenbach, D. J., & Tielens, A. G. G. M. 1999, RvMP, 71, 173
Hughes, A., Wong, T., Ott, J., et al. 2010, MNRAS, 406, 2065
Hunter, J. D. 2007, CSE, 9, 90
Indebetouw, R., Brogan, C., Chen, C.-H. R., et al. 2013, ApJ, 774, 73
Inoue, A. K., Tamura, Y., Matsuo, H., et al. 2016, Sci, 352, 1559
Israel, F. P. 1997, A&A, 328, 471
Israel, F. P., Johansson, L. E. B., Lequeux, J., et al. 1993, A&A, 276, 25
Israel, F. P., Johansson, L. E. B., Rubio, M., et al. 2003, A&A, 406, 817
Israel, F. P., & Maloney, P. R. 2011, A&A, 531, A19
Israel, F. P., Maloney, P. R., Geis, N., et al. 1996, ApJ, 465, 738
Jameson, K. E., Bolatto, A. D., Leroy, A. K., et al. 2016, ApJ, 825, 12
Jones, E., Oliphant, E., Peterson, P., et al. 2001, SciPy: Open source scientific tools for Python, http://www.scipy.org/
Kapala, M. J., Sandstrom, K., Groves, B., et al. 2015, ApJ, 798, 24
Kaufman, M. J., Wolfire, M. G., & Hollenbach, D. J. 2006, ApJ, 644, 283
Kaufman, M. J., Wolfire, M. G., Hollenbach, D. J., & Luhman, M. L. 1999, ApJ, 527, 795
Krips, M., Crocker, A. F., Bureau, M., Combes, F., & Young, L. M. 2010, MNRAS, 407, 2261
Kurt, C. M., & Dufour, R. J. 1998, RMxAC, 7, 202
Kurt, C. M., Dufour, R. J., Garnett, D. R., et al. 1999, ApJ, 518, 246
Langer, W. D., Velusamy, T., Pineda, J. L., Willacy, K., & Goldsmith, P. F. 2014, A&A, 561, A122
Le Petit, F., Nehmé, C., Le Bourlot, J., & Roueff, E. 2006, ApJS, 164, 506
Lee, C., Leroy, A. K., Schnee, S., et al. 2015, MNRAS, 450, 2708
Lee, L. 2017, NADA: Nondetects and Data Analysis for Environmental Data, R package version 1.6-1, https://CRAN.R-project.org/package=NADA
Leroy, A., Bolatto, A., Stanimirović, S., et al. 2007, ApJ, 658, 1027
Leroy, A. K., Bolatto, A., Bot, C., et al. 2009, ApJ, 702, 352
Leroy, A. K., Bolatto, A., Gordon, K., et al. 2011, ApJ, 737, 12
Leurini, S., Wyrowski, F., Wiesemeyer, H., et al. 2015, A&A, 584, A70
Madden, S. C., Poglitsch, A., Geis, N., Stacey, G. J., & Townes, C. H. 1997, ApJ, 483, 200
Madden, S. C., Rémy-Ruyer, A., Galametz, M., et al. 2013, PASP, 125, 600
Malhotra, S., Kaufman, M. J., Hollenbach, D., et al. 2001, ApJ, 561, 766
McMullin, J. P., Waters, B., Schiebel, D., Young, W., & Golap, K. 2007, adass XVI, 376, 127
Meixner, M., Panuzzo, P., Roman-Duval, J., et al. 2013, AJ, 146, 62
Mizuno, N., Yamaguchi, R., Mizuno, A., et al. 2001, PASJ, 53, 971
Muller, E., Ott, J., Hughes, A., et al. 2010, ApJ, 712, 1248
Muraoka, K., Homma, A., Onishi, T., et al. 2017, ApJ, 844, 98
Nikolić, S., Garay, G., Rubio, M., & Johansson, L. E. B. 2007, A&A, 471, 561
Nordon, R., & Sternberg, A. 2016, MNRAS, 462, 2804
Okada, Y., Requena-Torres, M. A., Güsten, R., et al. 2015, A&A, 580, A54
Ossenkopf, V., Röllig, M., Neufeld, D. A., et al. 2013, A&A, 550, A57
Ott, S. 2010, adass XIX, 434, 139
Padoan, P., Juvela, M., Bally, J., & Nordlund, Å. 2000, ApJ, 529, 259
Pagel, B. E. J. 2003, in ASP Conf. Ser. 304, CNO in the Universe, ed. C. Charbonnel, D. Schaerer, & G. Meynet (San Francisco, CA: ASP), 187
Paglione, T. A. D., Wall, W. F., Young, J. S., et al. 2001, ApJS, 135, 183
Pak, S., Jaffe, D. T., van Dishoeck, E. F., Johansson, L. E. B., & Booth, R. S. 1998, ApJ, 498, 735
Pilbratt, G. L., Riedinger, J. R., Passvogel, T., et al. 2010, A&A, 518, L1
Pineda, J. L., Langer, W. D., Goldsmith, P. F., et al. 2017, ApJ, 839, 107
Pineda, J. L., Langer, W. D., Velusamy, T., & Goldsmith, P. F. 2013, A&A, 554, A103
Planck Collaboration, Ade, P. A. R., Aghanim, N., et al. 2011, A&A, 536, A17
Poglitsch, A., Herrmann, F., Genzel, R., et al. 1996, ApJL, 462, L43
Poglitsch, A., Krabbe, A., Madden, S. C., et al. 1995, ApJ, 454, 293
Poglitsch, A., Waelkens, C., Geis, N., et al. 2010, A&A, 518, L2
Polk, K. S., Knapp, G. R., Stark, A. A., & Wilson, R. W. 1988, ApJ, 332, 432
Pound, M. W., & Wolfire, M. G. 2008, adass XVII, 394, 654
Requena-Torres, M. A., Israel, F. P., Okada, Y., et al. 2016, A&A, 589, A28
Reynolds, R. J. 1991, ApJL, 372, L17
Röllig, M., Ossenkopf, V., Jeyakumar, S., Stutzki, J., & Sternberg, A. 2006, A&A, 451, 917
Roman-Duval, J., Gordon, K. D., Meixner, M., et al. 2014, ApJ, 797, 86
Rubin, D., Hony, S., Madden, S. C., et al. 2009, A&A, 494, 647
Rubio, M., Elmegreen, B. G., Hunter, D. A., et al. 2015, Natur, 525, 218
Rubio, M., Garay, G., Montani, J., & Thaddeus, P. 1991, ApJ, 368, 173
Rubio, M., Lequeux, J., Boulanger, F., et al. 1993a, A&A, 271, 1
Rubio, M., Lequeux, J., & Boulanger, F. 1993b, A&A, 271, 9
Rubio, M., Lequeux, J., Boulanger, F., et al. 1996, A&AS, 118, 263
Russell, S. C., & Dopita, M. A. 1992, ApJ, 384, 508
Sandstrom, K. M., Bolatto, A. D., Bot, C., et al. 2012, ApJ, 744, 20
Sandstrom, K. M., Bolatto, A. D., Draine, B. T., Bot, C., & Stanimirović, S. 2010, ApJ, 715, 701
Sandstrom, K. M., Leroy, A. K., Walter, F., et al. 2013, ApJ, 777, 5
Schruba, A., Leroy, A. K., Kruijssen, J. M. D., et al. 2017, ApJ, 835, 278
Schruba, A., Leroy, A. K., Walter, F., et al. 2012, AJ, 143, 138
Shetty, R., Glover, S. C., Dullemond, C. P., et al. 2011, MNRAS, 415, 3253

Smith, J. D. T., Croxall, K., Draine, B., et al. 2017, ApJ, 834, 5
Smith, R. C. & MCELS Team 1999, in IAU Symp. 190, New Views of the
    Magellanic Clouds, ed. Y.-H. Chu et al. (San Francisco, CA: ASP), 28
Sofia, U. J., Cardelli, J. A., Guerin, K. P., & Meyer, D. M. 1997, ApJL,
    482, L105
Solomon, P. M., Sanders, D. B., & Scoville, N. Z. 1979, ApJL, 232, L89
Stacey, G. J., Geis, N., Genzel, R., et al. 1991, ApJ, 373, 423
Stacey, G. J., Smyers, S. D., Kurtz, N. T., & Harwit, M. 1983, ApJL, 265, L7
Stanimirović, S., Staveley-Smith, L., Dickey, J. M., Sault, R. J., &
    Snowden, S. L. 1999, MNRAS, 302, 417
Szűcs, L., Glover, S. C. O., & Klessen, R. S. 2016, MNRAS, 460, 82
Tayal, S. S. 2008, A&A, 486, 629
Tayal, S. S. 2011, ApJS, 195, 12
Tchernyshyov, K., Meixner, M., Seale, J., et al. 2015, ApJ, 811, 78
Temi, P., Marcum, P. M., Young, E., et al. 2014, ApJS, 212, 24
Tielens, A. G. G. M., & Hollenbach, D. 1985, ApJ, 291, 722
Van Der Walt, S., Colbert, S. C., & Varoquaux, G. 2011, arXiv:1102.1523
van Loon, J. T., Oliveira, J. M., Gordon, K. D., Sloan, G. C., &
    Engelbracht, C. W. 2010, AJ, 139, 1553
Velusamy, T., Langer, W. D., Pineda, J. L., & Goldsmith, P. F. 2012, A&A,
    541, L10
Wiesenfeld, L., & Goldsmith, P. F. 2014, ApJ, 780, 183
Wilson, T. L., & Rood, R. 1994, ARA&A, 32, 191
Wolfire, M. G., Hollenbach, D., & McKee, C. F. 2010, ApJ, 716, 1191
Wolfire, M. G., Hollenbach, D., McKee, C. F., Tielens, A. G. G. M., &
    Bakes, E. L. O. 1995, ApJ, 443, 152
Wolfire, M. G., McKee, C. F., Hollenbach, D., & Tielens, A. G. G. M. 2003,
    ApJ, 587, 278
Wong, T., Hughes, A., Tokuda, K., et al. 2017, ApJ, 850, 139
Wu, R., Polehampton, E. T., Etxaluze, M., et al. 2013, A&A, 556, A116